Towards quantifying contrails of fuel cell powered aircraft: first in-flight measurements of a fuel cell exhaust emulator

Simon Braun[1,4], Magdalena Pühl[1], Andreas Marsing[1], Daniel Sauer[1], Gregor Neumann[1], Elena de la Torre Castro[1,4], Valerian Hahn[1], Michael Lichtenstern[1], Paul Stock[1], Christopher Heckl[1], Dennis Hillenbrand[1,4], Anke Roiger[1], Christiane Voigt[1], Simon Unterstrasser[1], Arne Vasenden[2], Roberta Vasenden[2], Jean Cammas[3], Florian Thorey[3], Catherine Mackay[3], Charles Renard[3], and Tina Jurkat-Witschas[1]

[1]Deutsches Zentrum für Luft- und Raumfahrt, Institut für Physik der Atmosphäre, Oberpfaffenhofen, Germany
[2]AV Experts LLC, Denison, Texas, US
[3]Airbus Operations SAS, Toulouse, France
[4]Delft University of Technology, Faculty of Aerospace Engineering, Delft, The Netherlands

Correspondence: Simon Braun (simon.braun@dlr.de)

Abstract.

Aviation affects the climate through multiple pathways. The emission of carbon dioxide (CO_2) from conventional propulsion technologies has a warming effect, but also non-CO_2 effects like contrail cirrus play a crucial role. For new hydrogen (H_2) based propulsion concepts there are no direct CO_2 and soot emissions, but water vapor emissions are higher, which can affect contrail formation, micro-physical properties and climate impact. In-flight measurements of relevant contrail and emission parameters of fuel cell propulsion systems are non-existent. To study contrail formation in the wake of fuel cell powered aircraft, a fuel cell exhaust emulator (FCEE) was designed by Airbus to produce the low-temperature and high-humidity exhaust conditions expected from these systems. Due to their unique exhaust composition and thermodynamic emission characteristic, processes such as plume mixing with ambient air are crucial for understanding contrail formation. Further, to compare engine and fuel-dependent contrail properties, in situ methods derive a dilution-corrected apparent ice emission index (AEI_{ice}) using conservative tracers, such as CO_2 or nitrogen oxides (NO_X). As the FCEE does not emits such inert trace gas, a newly developed artificial dilution tracer system was used. The design and characterization of this system, as well as the significance and application for exhaust dilution and emission index assessment of fuel cell-powered aircraft in flight, are described.

As part of the Nephele flight test campaign in December 2023 in Minnesota, USA, the prototype FCEE and artificial dilution tracer release system were installed on board a Convair C131. The sampling system, together with instrumentation for emission and contrail measurement, were installed on a Piper Cheyenne 400LS chaser aircraft. Both aircraft were operated by AV Experts LLC. A proof-of-concept of the artificial tracer system was demonstrated during contrail and emission flights. Contrails formed on aerosol particles emitted by the FCEE near the homogeneous freezing threshold (at ambient temperatures around 230 K) were sampled at 400 hPa at distances of 50 to 1500 m behind the aircraft. An increase of AEI_{ice} from $1.4 \cdot 10^{13}$ to $4 \cdot 10^{15}$ $kg_{H_2}^{-1}$ with increasing temperature differences of 3 to 5 K below the homogeneous freezing temperature was observed. As contrails

from fuel cell systems form at higher ambient temperatures than those from conventional propulsion systems, these are the first contrail measurements in this temperature range. Complementary model simulations suggest that droplet freezing is responsible for the evolution of ice crystal numbers in this temperature range.

1 Introduction

The global increase in atmospheric carbon dioxide (CO_2) is the biggest contributor to anthropogenic climate change (Calvin et al., 2023). Aviation's share of global CO_2 emission in 2018 was around 2.4% (Lee et al., 2021). Besides CO_2, non-CO_2 effects of aviation, such as the formation of contrail cirrus and nitrogen oxides (NO_X) emissions, influence the climate. Although their global warming contributions are less well understood and subject to greater uncertainty, these studies suggest that their effective radiative forcing (ERF) may be twice as large as that of CO_2(Lee et al., 2021). CO_2 has a long residence time in the atmosphere and corresponding long-lasting radiative and climate impact. In contrast, non-CO_2 effects, in particular persistent contrails, have a short-term radiative effect in the order of 10-15 h (Kärcher, 2018). However, associated climate feedback effects may last for several decades (Borella et al., 2024; Bickel et al., 2025). A reduction in these effects therefore leads to an immediate reduction in aviation's warming contribution to the climate. In view of the strong expected growth in the aviation industry due to increasing air travel demand (Airbus, 2026; Boeing, 2026), the reduction of non-CO_2 effects is an important starting point for achieving the climate targets in aviation.

Current efforts to establish hydrogen as a new energy source in aviation are also putting the spotlight on non-CO_2 effects. Both the use of fuel cells and direct hydrogen combustion reduce direct CO_2 emissions to zero. However, the non-CO_2 effects remain relevant, with substantial uncertainties due to the lack of measurements. Model studies on the formation conditions of contrails from hydrogen-powered aircraft have already been carried out, but there are major uncertainties on the number of initially formed ice crystals and a lack of experimental validation (Schumann, 1996; Ponater et al., 2006; Gierens, 2021; Bier et al., 2024). The initial ice crystal number concentration in turn influences the total number of formed ice crystals and therefore the contrail lifetime (Lottermoser and Unterstrasser, 2026) and radiative forcing (Burkhardt et al., 2018). In view of the long development times in the aviation industry, it is important to improve our understanding of the topic in order to give early recommendations for current technologies (Voigt et al., 2026) and future development strategies for hydrogen propulsion concepts (Jurkat-Witschas et al., 2025).

In-flight in-situ measurements are an important approach to improve our understanding of the underlying effects of contrail formation. They can provide valuable data for improving and validating numerical models (Bier et al., 2022; Lewellen, 2020; Bier et al., 2024; Lottermoser and Unterstrasser, 2025a; Zink et al., 2026; Zink and Unterstrasser, 2026). This also supports climate impact assessments of new technologies (Gierens, 2021; Märkl et al., 2024) across entire fleets. For aircraft powered by hydrogen fuel cells no in-flight experiments have been carried out so far, due to the unavailability of testable emission sources. Besides the measurement of non-CO_2 emissions like water vapor, ice crystal number concentrations and NO_X, the main ambient parameters to assess contrail formation like temperature and relative humidity (RH) have to be quantified. Of particular importance is the determination of emission indices (EIs) of all relevant forcing parameters to compare different technologies

and fuels. An emission index relates the amount of the emitted species to the fuel consumption. It is therefore independent of plume dilution effects and compensates for inhomogeneity in the exhaust plume during in-flight measurements. An example of an EI is the apparent ice emission index (AEI_{ice}), which relates the number of ice crystals produced to the mass of fuel burned. Deriving an EI from airborne in-situ measurements requires an inert trace gas with a known concentration at the engine exit. This tracer must be measured simultaneously with the emission or contrail properties (e.g. the ice crystal number concentration). Assuming that the trace gas follows the same trajectories as the heavier ice or aerosol particles, the trace gas serves as a dilution tracer. For kerosene-powered aircraft, the emitted CO_2 is perfectly suited for this purpose. Its EI is easily determined beforehand based on the carbon content of the fuel and can therefore be used to calculate the EI of other emission parameters (Schulte and Schlager, 1996; ICAO, 2023). CO_2 has been used successfully for this purpose in past in-situ emission measurements (Moore et al., 2017; Voigt et al., 2021; Märkl et al., 2024). However, this approach is no longer applicable for hydrogen-powered aircraft, due to the absence of CO_2 as a combustion product. To overcome this limitation, a novel artificial dilution tracer system was developed and tested in flight. The aim of this system is to enable CO_2-independent dilution measurements needed to better understand contrail formation processes behind hydrogen-powered aircraft.

This article describes the setup, characterization and successful deployment of the novel artificial dilution tracer system, hereafter referred to as the ATReUS (Artificial Tracer Release Unit and Sampling) system. It was developed for fuel cell emission characterization during the flight test campaign "Nephele" in December 2023. The campaign aimed to test a prototype fuel cell exhaust emulator (FCEE), designed and operated by Airbus. The FCEE reproduces the exhaust conditions of a fuel cell in flight, allowing contrail formation in the nascent aircraft plume to be investigated. The test campaign took place in Minnesota, USA, in December 2023 and was led by Airbus. The German Aerospace Center (DLR) provided and operated the instruments for the contrail and emission measurements. A Convair C131 was used as the lead aircraft carrying the FCEE. In formation flights, the emissions and contrails behind the FCEE were measured by a Piper Cheyenne 400LS equipped with an emission and contrail measurement payload adapted to the aircraft. Both aircraft were operated by AV Experts LLC.

The collected data is used to compare the dilution properties of the FCEE to those of the gasoline-burning engines of the C131 and to characterize and validate the artificial dilution tracer concept. The AEI_{ice} of the FCEE is calculated from the data. The importance of an independent tracer system, which provides the means to quantitatively assess the mixing conditions behind the aircraft, is discussed. We explain why this is essential for measurements of non-CO_2 effects of hydrogen propelled aircraft and demo missions of hydrogen propulsion.

The conditions for droplet formation and freezing are inherently different in aircraft exhaust plumes from those occuring in nature as the time scales for nucleation and cooling are much shorter. For exhaust emissions without a strong initial jet velocity, the cooling rate may differ significantly from that of exhaust plumes from a strong jet (Lottermoser and Unterstrasser, 2025b). In order to study this effect, we additionally try to shed light on the freezing time scales for droplets in a fast cooling exhaust.

The development of the ATReUS system is described in Section 2. An overview of the Nephele flight test campaign and the measurement instruments used is provided in Section 3, including a description of the FCEE design and the procedure for contrail prediction and flight planning. The results of the trace gas and contrail ice analysis are discussed in Section 4.

2 Development of the Artificial Tracer Release Unit and Sampling system (ATReUS)

The lack of CO_2 in the exhaust of hydrogen based propulsion technologies and thus the lack of a dilution tracer prompted the development of the ATReUS system for dilution measurements. A schematic of the working principle is shown in Fig. 1 (a). The general idea is to release a trace gas that is well mixed with the exhaust of the emission source. The trace gas and the emission species in the plume of the lead aircraft are then measured co-located by the chaser aircraft. This allows the quantification of dilution effects and the calculation of an EI value. In the case of the Nephele flight test campaign, the artificial dilution tracer was released inside the FCEE, approximately $8\,\mathrm{m}$ upstream of its exhaust plane. This ensures that the artificial dilution tracer is well mixed with the FCEE airflow at the exhaust. The artificial dilution tracer is clearly distinguishable from other emission species produced during combustion like the CO_2 emitted by the engines of the carrier aircraft and can therefore be used to identify the exhaust plume of the FCEE.

Finding a suitable trace gas for this application is the first step in the design process. N_2O was chosen here. This is followed by an investigation on dimensioning and the operational scope of the release subsystem, based on tracer measurements of previous flight experiments. Then a N_2O sensor is selected and modified for aircraft measurements (in this case a LI-7820 N_2O/H_2O Trace Gas Analyzer by LI-COR). The environmental impact of the tracer system is assessed and the methodology of calculating EI values based on the artificial dilution tracer provided. By comparison with the established dilution tracer CO_2 a proof of principle is provided in Section 4.

2.1 Selection of a suitable trace gas

The first step in designing the ATReUS system, is the selection of a suitable trace gas. Here, nitrous oxide (N_2O) is chosen for this application: It has a low ambient background mole fraction of about 330-340 ppbv in the middle troposphere (Tian et al., 2024), ensuring that only a small amount of gas has to be released in order to obtain an adequate mole fraction enhancement above the background. Additionally, due to its long atmospheric lifetime, it is essentially homogeneously distributed in the upper troposphere (Krysztofiak et al., 2023), where the test flights take place. This enables clear identification of the emitted species without complicated and error prone corrections of the background. Furthermore, no phase changes or chemical decomposition of N_2O are expected in the considered exhaust conditions. We note here that N_2O can also be produced in small quantities during combustion processes. Santoni et al. (2011) quantified this effect for the NASA DC-8 aircraft at 30 to 100% thrust setting during the first Alternative Aviation Fuel Experiment (AAFEX-I) in 2009. They derived an EI of $32 \pm 18\,\mathrm{mg}$ N_2O per kg of JP-8 fuel. Therefore, the released quantity has to be kept well above this in order to clearly identify emission sources in case combustion sources are involved.

N_2O is used in different industries, e.g. narcotics, and is therefore relatively cheap and easily available. This reduces costs as well as uncertainty regarding the trace gas supply especially during campaigns. Additionally, N_2O is non-toxic and can be easily stored in a pressurized bottle, either gaseous or liquefied. But, because it is a potent oxidizer, careful handling is required for its storage and use. Also, CO_2 and N_2O have similar molar masses and therefore similar diffusion speeds (Graham, 1995). This is particularly important for measurements taken at distances of several kilometers between the lead and chaser aircraft, as

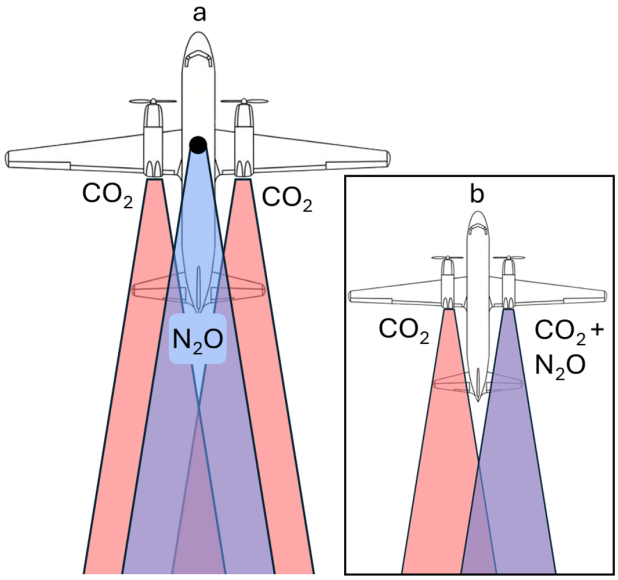

Figure 1. a: Concept of the artificial dilution tracer system: the controlled release of a trace gas, that is not attributable to combustion processes in the quantities released, in this case N_2O, makes it possible to identify the emission source and distinguish the plume of the FCEE (blue) from the exhaust plumes of the main engines (red). b: Proof-of-concept experiment, in which the tracer was released close to the engine exhaust, to directly compare the dilution characteristics of the artificial dilution tracer with CO_2 emitted from the engines (see also 4.1).

diffusion processes play an important role there (Lottermoser and Unterstrasser, 2025b) and comparability with past measurements, that use CO_2 as dilution tracer, must be maintained. Another factor is the availability of detectors that can capture the variable conditions and large gradients of the tracer in the plume. In the case of N_2O, different sensors are commercially available due to its relevance as a greenhouse gas in the industrial and agricultural sectors. The adaptation to flight measurements in turbulent conditions was the main challenge here. To summarize, the combination of release and detection mechanism in terms of availability, safety, ambient background concentrations and detectability provided conclusive arguments to use N_2O as the trace gas for our application.

2.2 Design of the tracer release unit

The design goal of the tracer release unit is to generate N_2O enhancements over the ambient mole fraction ($\Delta r_{\mathrm{N_2O}}$) within the measurement range of the sampling instrument over a large range of plume samples at varying distances and mixing stages. The necessary amount of N_2O trace gas released into the exhaust flow is estimated by taking the relevant boundary conditions into account: the targeted measurement distances, the total flow of the emitted exhaust gases (in this case the mass flow through the FCEE), the background variability of ambient N_2O, as well as a detection limit of the N_2O sensor.

For our experiment, a maximum distance of 1500 m between lead and chaser aircraft was chosen as the relevant target distance

range, thus the system was mainly tuned to near-field measurements. The limit of quantitation (LOQ) for the N_2O sensor of 4 ppbv was set conservatively at ten times the standard deviation (of 0.4 ppbv according to the manufacturer for 1 Hz averaged data, more details on the selection process of the N_2O sensor can be found in Section 2.3). To compensate for variability of the ambient N_2O mole fraction and to account for the novelty of the concept, this budget was doubled. The estimated combined detection limit is therefore 8 ppbv. Using the empirical dilution law derived by Schumann (Schumann et al., 1998), which is based on past in-flight dilution measurements, the necessary minimum N_2O mass flow was estimated. The detection limit and the expected enhancements over background at the respective plume centers are shown in Figure 2. The black lines represent the expected tracer enhancements for a given initial exit mole fraction over the distance between measurement and point of emission. Based on this study the minimum necessary N_2O mole fraction at the exhaust plane of the FCEE was estimated to be 610 ppmv (comparable to the dashed line in Figure 2). Assuming a total air mass flow of $0.2\,\mathrm{kg\,s^{-1}}$ through the FCEE, the initial tracer release was set to 6 slpm (liter at atmospheric pressure and 0 °C per minute) or $1.98 \cdot 10^{-4}\,\mathrm{kg\,s^{-1}}$ of N_2O following this analysis.

Two mass flow controllers (MFC) from Bronkhorst, with a combined maximum nitrogen equivalent flow of 15 slpm provide the precisely set mass flow of N_2O. This setup allows for an adjustment range from 0.5 to 10.5 slpm N_2O. The two MFCs are installed inside a standard 19" slide-in, together with a data logger and two MFC adjustment dials to enable in-flight N_2O mass flow adjustments (Fig. 3). The slide-in is supplied with 28 VDC and a constant pure N_2O gas flow with an inlet pressure of 2-3 bar. The gas supply was realized with a gas bottle filled with highly purified (99.998%), liquefied N_2O. 1/4-inch PFA (Perfluoroalkoxy alkane) tubes are used for the N_2O plumbing between gas supply, slide-in and tracer outlet. For the tracer outlet a 1/4-inch stainless steel tube with a 90° bend in flow direction was installed centered inside the FCEE heated air supply. During the Nephele flight test campaign the N_2O mass flow was increased to $9.33\,\mathrm{slpm}/3.08 \cdot 10^{-4}\,\mathrm{kg\,s^{-1}}$ (90% of the maximum flow rate) achieving a mean mole fraction of 845 ppmv at the exhaust plane of the FCEE. This adjustment was made to increase $\Delta r_{\mathrm{N_2O}}$ and achieve better detection of the FCEE exhaust plume.

2.3 Selection and modification of a N_2O sensor for ATReUS

Due to its atmospheric importance as a strong greenhouse gas and most important ozone-depleting substance, a variety of N_2O measurement systems are commercially available. Significant progress has been made recently, particularly in the field of laser spectroscopy, with many instruments already having been successfully tested in flight (Pitt et al., 2016; Gvakharia et al., 2018; Waldmann et al., 2026). The sensor of the sampling subsystem of ATReUS must be precise at ambient N_2O mole fractions. Ideally it should cover a dynamic range of up to 100 to 1000 times the atmospheric mole fraction of 337 ppbv (global mean, NOAA, Lan et al. (2026)). A stable instrument, with minimal internal drift, cross sensitivities and changes in the sensitivity is advantageous. This avoids the need for in-flight calibration measurements and thereby reduce system complexity and weight. Additionally, the sensor should be compact and light. To realize a high temporal resolution which is required for airborne emission measurements with large gradients, a high sampling frequency is needed. For the formation flights and the associated close distance exhaust plume encounters large gradients of water vapor concentrations are to be expected (background to in-plume). An additional capability to measure H_2O is therefore desired, to correct for cross-sensitivity effects.

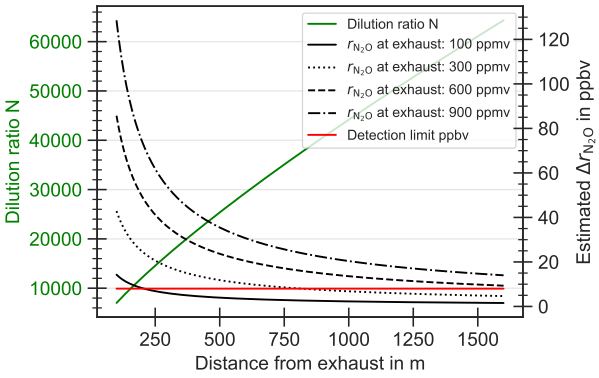

Figure 2. Estimated dilution rates of an artificial N_2O tracer, based on past in-flight dilution measurements of commercial aircraft (Schumann et al., 1998); The dilution ratio N according to Schumann et al. (1998) is displayed in green over the corresponding distance between exhaust exit plane and sampling inlet for an estimated aircraft speed of $100\,\mathrm{m\,s^{-1}}$. The black lines indicate the evolution of the N_2O enhancements above the atmospheric background Δr_{N_2O} for different N_2O mole fractions at the FCEE exhaust. The red line represents the detection limit of $7\,\mathrm{ppbv}$ of the in-flight sampling system.

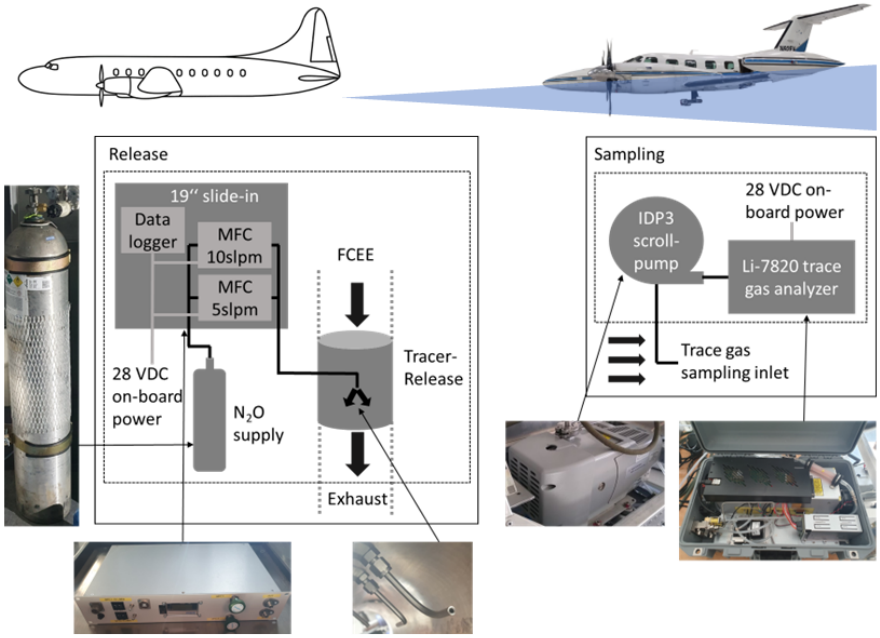

Figure 3. System architecture of the ATReUS system; the release subsystem was installed on the Convair C131 lead aircraft. The sampling subsystem was installed on the Cheyenne Piper 400LS chaser aircraft and is shown on the right.

Ultimately the LI-7820 N_2O/H_2O Trace Gas Analyzer by LI-COR, Inc. was selected because it meets these requirements. It uses the optical feedback cavity enhanced absorption spectroscopy (OF-CEAS) technique to derive the concentrations of N_2O and H_2O from their optical absorption characteristics inside an optical cavity. Here, light reflected back from the cavity to the laser facet acts as an external source of injection seeding, leading to laser-cavity resonance, thereby reducing the linewidth of the laser source emission and enhancing the signal intensity. The molecular absorption properties of the sample gas are evaluated at different wavelengths, which correspond to the resonance frequencies of this laser-cavity feedback effect. The sensor has a sampling rate of 1 Hz. Its compact size and low weight are well suited for an aircraft installation.

The sensor housing was modified to fit into a DLR Falcon 20 instrument rack, and an additional scroll pump was installed to enable measurements at the low pressures encountered during flights (Fig. 3). The N_2O sensor was characterized beforehand in this configuration. It was found that the additional scroll pump did not affect the quality of the measurement but reduced the residence time in the inlet line. The precision of 0.4 ppbv at 330 ppbv provided by the manufacturer was validated under laboratory conditions. For dry gas with constant composition an even better precision of 0.1 ppbv was observed. This was found to be well suited for the intended purpose. The instrument drift was determined to be 0.2 ppbv over a time of 13 h. In view of the expected duration of the measurement flights of up to 5 h, this means that no in-flight calibration is needed to compensate for instrument drift. To ensure comparability to other instruments and data sets all measurements are referenced to an international standard. The calibration strategy is described in Appendix A. For the Nephele flight test campaign the inlet of the ATReUS sampling system was realized with 2.5 m of PFA ¼' tubing. The inlet itself was installed next to the inlets for the relevant emission measurements. All trace gas and aerosol inlets are positioned at a distance of 40 cm to the CAPS ice particle probe mounted on the belly of the chaser aircraft (as shown in Fig. 4). Close proximity of the sampling inlets allows for a more precise dilution correction, by reducing radial dilution effects and uncertainty related to the aerodynamic influence of the chaser aircraft's structure. With this setup, no losses are expected for the N2O measurements. The response time is estimated as < 0.5 s.

2.4 Calculation of Emission Indices and other dilution-corrected metrics based on the artificial dilution tracer

EIs are calculated to assess emissions independently of dilution due to atmospheric mixing of the measured exhaust plume with ambient air and due to spatial inhomogeneities inside the exhaust plume itself. They relate the quantity of an emission to the consumed fuel mass. This allows comparisons to be made between different operating conditions and also between different aircraft types and propulsion technologies with regard to their emissions. In addition, they make it possible to estimate the total emission mass, based solely on fuel consumption.

EI for the artificial N_2O tracer can be calculated directly using a mass flow ratio as shown in equation 1. Here, $\dot{m}_{\mathrm{N_2O}}$ is the released N_2O mass flow and $\dot{m}_{\mathrm{ref}}$ is a reference mass flow. The reference mass flow can be chosen in such a way that the best comparability can be established, depending on the respective application. For example, in the case of an implementation of the artificial dilution tracer in a fuel cell system, the hydrogen consumption is a logical choice.

$$EI_{\mathrm{N_2O}} = \frac{\dot{m}_{\mathrm{N_2O}}}{\dot{m}_{\mathrm{ref}}} \tag{1}$$

$$EI_X = \frac{\Delta X \cdot S(X)}{\Delta r_{\mathrm{N_2O}}} EI_{\mathrm{N_2O}} \tag{2}$$

$$S(X) = \begin{cases} V_m / M_{\mathrm{N_2O}} & \text{for particles} \\ M_X / M_{\mathrm{N_2O}} & \text{for trace gases} \end{cases} \tag{3}$$

By providing an EI for the artificial dilution tracer, the EIs of all other emissions can be derived using equations 2 and 3, adapted from Moore et al. (2017). This requires the N_2O concentration enhancement over background ($\Delta r_{\mathrm{N_2O}}$), the molar mass of N_2O ($M_{\mathrm{N_2O}}$) and the measured concentration enhancement (ΔX) of the species X for which the emission index is calculated. In the case of particle measurements, V_m is the molar volume of ideal gas at standard temperature and pressure and in the case of trace gas measurements, M_X is the molar mass of species X. It is important to note that all resulting EIs calculated from this refer to the reference mass flow used in equation 1 accordingly. EI calculated in this way depends heavily on the reference mass flow used, which must therefore always be specified. When comparing the EI of hydrogen and kerosene combustion systems, it makes sense to normalize the hydrogen EI on the basis of the ratio between the energy contents of both fuels. This is done by dividing the EI value by the energy content per fuel mass, thereby relating the emissions metric directly to the energy released during combustion. A hydrogen-based EI value can be compared to kerosene-based EIs by applying a factor of 0.36 (ratio of the specific combustion heat of both fuels according to Schumann (1996)).

For the Nephele flight test campaign, it was decided to use a hypothetical hydrogen mass flow as the reference mass flow for EI calculation. Taking into account a stoichiometric ratio, the hypothetical amount of hydrogen consumed was calculated from the amount of water emitted. The reaction is shown in equation R1: two hydrogen molecules react with an oxygen molecule to form water. Equation 4 indicates the reaction mass balance, taking the molar masses of all reactants into account. Finally, the calculation of the reference mass flow is displayed in equation 5. The water vapor mass flow $\dot{m}_{\mathrm{H_2O\,vapor}}$ going through the fuel cell emulator was monitored during the flight experiments.

$$2H_2 + O_2 \rightarrow 2H_2O \tag{R1}$$

$$1gH2 + 7.938gO2 = 8.938gH2O \quad (M_{\mathrm{H_2}} = 2.016\,\mathrm{g\,mol^{-1}}, M_{\mathrm{O_2}} = 31.999\,\mathrm{g\,mol^{-1}}, M_{\mathrm{H_2O}} = 18.015\,\mathrm{g\,mol^{-1}}) \tag{4}$$

$$\dot{m}_{\mathrm{ref}} = \dot{m}_{\mathrm{H_2hyp}} = \frac{\dot{m}_{\mathrm{H_2O\,vapor}}}{8.938} \tag{5}$$

Here, $M_{\mathrm{H_2}}$, $M_{\mathrm{O_2}}$ and $M_{\mathrm{H_2O}}$ are the molar masses of hydrogen, oxygen and water. $\dot{m}_{\mathrm{H_2hyp}}$ is the hypothetical hydrogen mass flow and $\dot{m}_{\mathrm{H_2O\,vapor}}$ the water vapor mass flow through the FCEE, assuming no additional liquid water is emitted.

Additionally, the artificial dilution tracer allows a direct estimation of the concentration of an emitted species at the exhaust. This can be done by quantifying the exhaust plume dilution with ambient air at the point of sampling. For this the mole fraction of the artificial dilution tracer at the emission source needs to be monitored. By relating this to the $\Delta r_{\mathrm{N_2O}}$ sampled by the chaser aircraft, a dilution factor N_{dil} can be calculated directly (see equation 6). N_{dil} on the other hand can be used to estimate the concentration of any additionally measured species X at the exhaust exit plane. Furthermore, in the case of contrail ice crystals, the respective number concentration at the exhaust exit plane can then be used to calculate the number of formed ice crystals per flight meter (see equation 7).

$$N_{\mathrm{dil}} = \frac{\Delta r_{\mathrm{N_2O}}}{r_{\mathrm{N_2O_ex}}} = \frac{\Delta r_{\mathrm{N_2O}} \cdot \dot{m}_{\mathrm{air}} \cdot M_{\mathrm{N_2O}}}{\dot{m}_{\mathrm{N_2O}} \cdot M_{\mathrm{air}}} \tag{6}$$

$$N_{\mathrm{ice_fm}} = N_{\mathrm{dil}} \cdot N_{\mathrm{ice}} \cdot A_{\mathrm{ex}} \tag{7}$$

Here N_{dil} is the dilution factor, $\Delta r_{\mathrm{N_2O}}$ is the measured enhancement of N_2O mole fraction above the atmospheric background, $r_{\mathrm{N_2O_ex}}$ is the mole fraction of the artificial dilution tracer at the exhaust of the emission source. $\dot{m}_{\mathrm{air}}$ is the total mass flow through the FCEE with the corresponding molar mass M_{air}. Likewise, $\dot{m}_{\mathrm{N_2O}}$ is the released N_2O mass flow with the corresponding molar mass $M_{\mathrm{N_2O}}$. $N_{\mathrm{ice_fm}}$ is the number of emitted ice crystals per flight meter (in $\mathrm{m^{-1}}$), N_{ice} is the measured ice crystal number concentration (in $\mathrm{m^{-3}}$) and A_{ex} is the surface area of the exhaust (in $\mathrm{m^2}$). Like the calculation of $\mathrm{AEI_{ice}}$ with the help of the artificial dilution tracer, this approach is only viable, if the measured species X can be clearly assigned to an emission source. This enables a unique evaluation of dilution-corrected emission parameters, which would not be possible without the artificial dilution tracer.

2.5 Environmental Assessment

N_2O is the third-most-important human-emitted greenhouse gas (Calvin et al., 2023). N_2O perturbations have an effective residence time of 109 years (Prather et al., 2015). According to the IPCCs Sixth Assessment Report (Forster et al., 2023), N_2O has a global warming potential (GWP) of 273 ± 130 over a 100 year time horizon. Therefore, the emission of N_2O, which is used as the artificial dilution tracer in this case, has to be assessed in terms of its climate impact.

During the Nephele flight test campaign in December 2023, the artificial N_2O tracer was used during five flight tests for an approximate total duration of 11 h. Considering a gas flow of 9.5 slpm, a total mass of 11.5 kg N_2O was released. This corresponds to an equivalent CO_2 emission of 3140 kg, or the CO_2 emission of burning one metric ton of kerosene (in terms of $\mathrm{GWP_{100}}$). For context, this is less CO_2 than emitted by three scientific personnel traveling from Germany to the US and back to conduct the flight test campaign (assuming a direct connection via a wide-body aircraft 80% full). A better understanding of the underlying contrail forming processes and a resulting potential reduction in non-CO_2 effects in the future, justify this



Figure 4. Chaser aircraft: Piper Cheyenne 400LS operated by AV Experts LLC, with instruments installed and operated by DLR. All instruments except the cloud probe were installed inside the cabin. Trace gas and aerosol inlets were placed next to the cloud probe below the aircraft's fuselage.

contribution. Still, the climate impact shall not be neglected and must be assessed for future uses of N_2O as an artificial dilution tracer.

3 The Nephele flight test campaign

Two aircraft were modified for the Nephele flight test campaign carried out in December 2023 led by Airbus. The lead aircraft, a Convair C131 powered by two Pratt & Whitney R-2800 Double Wasp radial aircraft engines owned and operated by AV Experts LLC, carried the ATReUS release subsystem and the FCEE designed and operated by Airbus. The chaser aircraft, a Piper Cheyenne 400LS, owned and modified by AV Experts LLC was equipped with atmospheric measurement instrumentation by DLR. Both aircraft were operated by AV Experts LLC, Texas (USA).

Close distance formation flights (approx. 50-1500 m longitudinal distance) up to an altitude of 25000 ft MSL were performed. The goal of the Nephele flight test campaign was to test and characterize the artificial dilution tracer as well as the FCEE. Accordingly, the measurement payload on the chaser aircraft measured all relevant FCEE emission and contrail parameters, relevant ambient parameters, the artificial dilution tracer and CO_2 emissions from the C131's engines. A total of four formation flights were performed in Minneapolis, Minnesota. One additional formation test flight as well as a single instrument test flight were performed in Denison, Texas.

Table 1. Atmospheric measurement instrumentation used during the flight tests on the Piper Cheyenne 400LS chaser aircraft

Instrument Name	Measurement Metric, range	Short description
Waran	H_2O, 50-10000 ppmv	Tunable diode laser hygrometer
CR-2	H_2O, 1-20000 ppmv	Frostpoint hygrometer
Licor-7000	CO_2 (and H_2O), 0-3000 ppmv	Differential, Non-Dispersive Infrared (NDIR) gas analyzer
Licor-7820	N_2O (and H_2O), 0-100 ppmv	Optical Feedback Cavity-Enhanced Absorption Spectrometer
CAPS CAS-DPOL	Ice particle size distribution, 0.5-50 µm	Light scattering probe
CAPS CIP	Ice particle size distribution, 15-900 µm	Optical shadow imaging probe
CAPS PT100	Temperature, calibrated range 235-295 K	Thermistor
aMCPC	Aerosol number conc. > 7 nm	advanced Mixing Condensation Particle Counter
aMCPC + thermodenuder[1]	Non-vol. aerosol number conc. > 7 nm	advanced Mixing Condensation Particle Counter
SEMS	Particle Size Distribution, 5-350 nm	Scanning Electric Mobility Sizer
Grimm SkyOPC	Particle Size Distribution, 0.25-2.5 µm	Optical Particle Counter

[1] setpoint 230 °C

The instruments were installed on the Cheyenne chaser aircraft by AV Experts LLC. and operated by the Institute of Atmospheric Physics, DLR.

3.1 Atmospheric measurement instrumentation

DLR and AV Experts LLC equipped the Cheyenne Piper chaser aircraft with the necessary instrumentation for the in-flight emission and contrail measurements. The instruments used during the Nephele flight test campaign are listed in Table 1 and shown in Fig. 4. The ice particle sensors are housed inside an externally mounted probe positioned at the bottom of the fuselage. The remaining instrumentation is installed in the cabin of the Piper Cheyenne and connected to stainless steel inlet tubes positioned in close proximity to the ice particle probe. A forward facing inlet was used for the aerosol measurements and backward-facing inlets for the trace gas and water vapor measurements.

The CAPS probe, short for Cloud, Aerosol and Precipitation Spectrometer, is used to measure the ice particle number concentration and size distribution. These are important parameters for understanding the underlying process of contrail formation. The number of ice crystals initially formed in the plume has a strong impact on the contrail cirrus climate relevant properties as it determines the optical and radiative properties and the lifetime of the contrail (Burkhardt et al., 2018; Lottermoser and Unterstrasser, 2026). The CAPS is comprised of two sensors: The Cloud Imaging Probe (CIP) uses optical imaging by focusing an incident laser beam on particles in the size range from 15 to 900 µm. The Cloud and Aerosol Spectrometer (CAS) uses particle light scattering to determine particle sizes in a size range from 0.5 to 50 µm. Additionally, the CAPS is equipped with

sensors for ambient temperature, static pressure, and dynamic pressure. The temperature measurement, particularly important for the contrail ice analysis, uses a thermistor with 1 K accuracy and a precision of 0.2 K.

Together with temperature measurements, the water vapor instruments are used to assess ambient relative humidity with respect to ice (RHi) and water (RHw), as well as the water vapor content inside the exhaust plumes of both the engines and the FCEE. The ambient RH has an influence on the threshold temperature for droplet formation and is a critical parameter for contrail persistence (Schumann, 1996). The WAter vapoR ANalyzer (Waran) is a tunable diode laser hygrometer. It utilizes the optical absorption of the 1.37 µm line from an indium–gallium–arsenide tunable diode laser to determine the water vapor concentration in the sample flow. It can measure water vapor in the range from 50 to 10000 ppmv, with a precision of 5% or 50 ppmv, whichever is greater (Marsing et al., 2023). With its internal sampling rate of 4 Hz rapid changes in concentration can be mapped as they occur during sampling of an exhaust gas jet. The CR-2 (Buck Research Instruments, LLC) is the second water vapor instrument, used for measurements of ambient water vapor. It uses a mirror with a precise temperature control to measure the frost point of the sampled air. The CR-2 measures in a range of 1 to 20000 ppmv, with an accuracy of 9% and precision of 1% in the 50-500 ppmv range (Heller et al., 2017). It cannot resolve fast changes in water vapor concentration due to the inertia of the mirror's temperature control, but is stable over a long measurement period. The CR-2 is therefore used for measurements of the background water vapor and serves as a comparison to the Waran. The combination of both enables highly accurate measurements with a sufficiently high sampling rate. Both Waran and CR-2 are installed inside an instrument rack mounted in the aircraft cabin. The backward-facing inlets for both instruments are mounted underneath the main fuselage, close to the CAPS instrument. Both instruments are regularly calibrated against a reference MBW 373LX dew point mirror.

The aerosol instrumentation is installed inside the so-called Aerosol-Box (A-Box), mounted in the cabin of the aircraft. They are used to measure volatile and non-volatile particles and particle size distribution in the sample air. The aerosol instrumentation described below was installed previously aboard a Grob G 520 Egrett, with the only difference being, that it was installed in a pressurized cabin during the Nephele flight test campaign. For more detailed information about the instruments see Neumann et al. (2025). During the Nephele flight test campaign ambient aerosol concentrations as well as soot from the engines from the lead aircraft are measured. The aerosol measurement payload is comprised of two advanced mixing condensation particle counters (aMCPC) measuring particles larger than 7 nm. One is used to measure total particle concentrations. The other aMCPC is equipped with an upstream thermodenuder to measure non-volatile particle concentrations. The thermodenuder was operated at an evaporation temperature of 230 °C. Its evaporation performance was characterized in Neumann et al. (2025) using tetracontane, for which 100% evaporation was observed for particles up to 80 nm. A scanning electric mobility sizer (SEMS) combined with an additional aMCPC, was implemented to measure particle size distributions. For measurement of larger aerosols in the size range of 0.25-2.5 µm an optical particle counter (OPC) was installed. A forward-facing inlet is used to collect the sampling air in close proximity to the CAPS probe. An additional backward-facing inlet is provided to switch the sampling air flow in the event of ice formation blocking the forward-facing inlet. Ultimately the forward-facing inlet was used, as icing did not impair the measurement at any point.

The trace gas instruments are used to measure the emission tracers CO_2 and the artificial dilution tracer N_2O. The LiCor Li-7000 CO_2 sensor is installed inside the A-Box. It uses infrared laser absorption to measure CO_2 and H_2O. The Li-7000 is

comprised of two sample cells, one measuring the sample air and the other constantly measuring synthetic air as a reference to derive the samples mole fraction through a comparison of both absorption rates. The additional H_2O measurement is used for a water vapor correction. The Li-7000 as part of the A-Box was also used previously aboard a Grob G 520 Egrett, for more detail see Neumann et al. (2025). The N_2O sensor, a LiCor Li-7820, is installed inside the instrument rack together with the water vapor instrumentation, as part of the ATReUS system. More detail about it can be found in section 2.3. Both the CO_2 and N_2O backward facing sample inlets were installed next to the CAPS probe on the bottom of the fuselage, as depicted in Fig. 4. During the Nephele flight test campaign two secondary standards for CO_2 and two secondary standards for N_2O in the form of calibration gas bottles were used for regular calibrations to compensate for instrument drift and to increase accuracy (described in Appendix B). The calibration gas bottles were sampled during the flight in the case of the CO_2 instrument and before and after each flight in the case of the N_2O instrument. All secondary standards used during the Nephele flight test campaign were previously referenced to primary low and high gas standards provided by NOAA (Kitzis, 2017).

The uncertainty of the measurements of both instruments is expressed by the combination of an absolute and a relative error. In case of the Li-7820, the instrument precision and the reproducibility of the standards are taken into account. The same applies to the Li-7000, but here sensitivity to water vapor is also considered by applying a correction for water vapor dilution. The total uncertainty for the Li-7820 is the sum of $0.27\,\mathrm{ppbv}$ absolute and 0.04% relative uncertainty and for the Li-7000 the sum of $0.28\,\mathrm{ppmv}$ absolute and 0.08% relative uncertainty.

All instruments were connected using a network switch to synchronize to GPS time. Furthermore, a forward-facing camera was installed inside the cockpit to enable a visual inspection of both distance and the formation of contrails. A differential GPS system (DGPS) installed on the emission and sampling aircraft is provided by Airbus for precise distance measurements. The system was used to help the pilots gauge the distance between lead and chaser aircraft during the flight, by displaying it in the cockpit. It also provides detailed positioning data for the post-measurement analysis.

3.2 Fuel cell exhaust emulator

The fuel cell exhaust emulator (FCEE) is designed to emulate the exhaust composition expected from future hydrogen fuel cell propulsion systems. It was designed by Airbus and built according to the design of Airbus. AV Experts LLC adapted and installed the system onboard their Convair C131 aircraft for the Nephele flight test campaign. The FCEE is intended for deployment during flight tests to evaluate and characterize contrail formation processes and properties under representative atmospheric conditions, without the need for a complex hydrogen system. The exhaust conditions probed during the Nephele flight test campaign mainly serve the purpose of exploring different contrail formation mechanisms and ways to suppress these as potential future mitigation options. For this purpose, liquid water is evaporated in a hot air stream to generate high humidities at the exhaust. The exhaust humidity can be adjusted, by changing the amount of injected water, with a targeted exhaust gas composition of 100% RHw at $34\,^{\circ}\mathrm{C}$. The hot air is supplied by the Convair C131 aircraft, utilizing the waste heat of the exhaust stack of its engines. It is redirected from the anti-ice system to the emulator. Water is sprayed into this hot air stream and vaporized inside of the evaporation chamber, mounted under the fuselage (shown in Figure 5). The water flow is achieved by pressurizing a water tank with nitrogen and regulated by valves. The system has two nozzles for spraying the water at different

positions in the evaporation chamber. Additionally, the emulator is equipped with sensors to monitor and record the relevant system parameters, like the exhaust gas temperature, humidity and total air mass flow.

The emulator consists of:

- An evaporation chamber that allows water droplets to mix with the hot air stream and to vaporize. The length of the evaporation chamber is defined by the time needed to evaporate 100% of the liquid water. This lowers the temperature of the air stream from 220 °C to as low as approximately 30 °C.
- A droplet spray system producing micrometer-sized water droplets (up to $30\,\mathrm{g\,s^{-1}}$). The evaporation chamber diameter is sized to reduce the interferences between the droplet spray and the chamber walls.
- A system providing pressurized water (at $70\,\mathrm{bar}$) to the spray system's nozzles.
- Temperature and pressure sensors that monitor the conditions inside of the evaporation chamber.

It should be noted here that the system was only deployed during a two-week campaign for a total of 5 test flights carried out in relevant atmospheric conditions. A contamination in the hot air supplying the emulator was identified, either coming from unfiltered air or oil contamination in the system. Total particulate matter (tPM) number concentrations greater than $3{\cdot}10^6\ \mathrm{cm^{-3}}$ were measured inside the FCEE. During inspection of the FCEE's ducts, traces of oil were found on the inner surfaces, which are therefore the most likely source of the particles. The oil contamination most likely originates from hot, oil-coated surfaces in the C131's engines, close to the hot-air intake for the FCEE. Model simulations by Zink et al. (2025) show that small amounts of oil (in the order of $\mathrm{ml\,h^{-1}}$) can cause high number concentrations of oil particles that act as precursors for contrail ice crystals (Ponsonby et al., 2024). In our experiment, we determined the number of aerosol particles in the hot supply air but not the type or size. While the original design targets for the FCEE regarding exhaust humidity (0 to 100% RHw) and temperature (30 to 60 °C) were met, the goal of producing a particle-free exhaust was not achieved. Consequently, it is not comparable with an actual fuel cell system. Nevertheless, we use the data to explore the high-humidity, low-temperature conditions with classical formation pathways involving exhaust type particles to explore the droplet freezing near the homogeneous freezing threshold.

3.3 Weather predictions for persistent contrails

A contrail is composed of ice crystals, which form behind the aircraft at high altitude, when local conditions are favourable. Droplets are first formed when saturation with respect to liquid water is met in the aircraft plume, and then these droplets freeze, if the temperature is low enough. The contrail persists as long as it remains in an ice supersaturated region (ISSR), a local atmospheric air mass characterised by low temperature and a humidity level that is super-saturated with respect to ice.
Prior to the flight campaign, and in order to choose the ideal location for the flight tests, statistics on ISSRs using multiple years of ERA5 ECMWF (European Center for Medium-Range Weather Forecasts) data, for different months and geographical areas in the US were calculated. Results clearly identified geographical areas where the frequency of ISSRs was highest, including

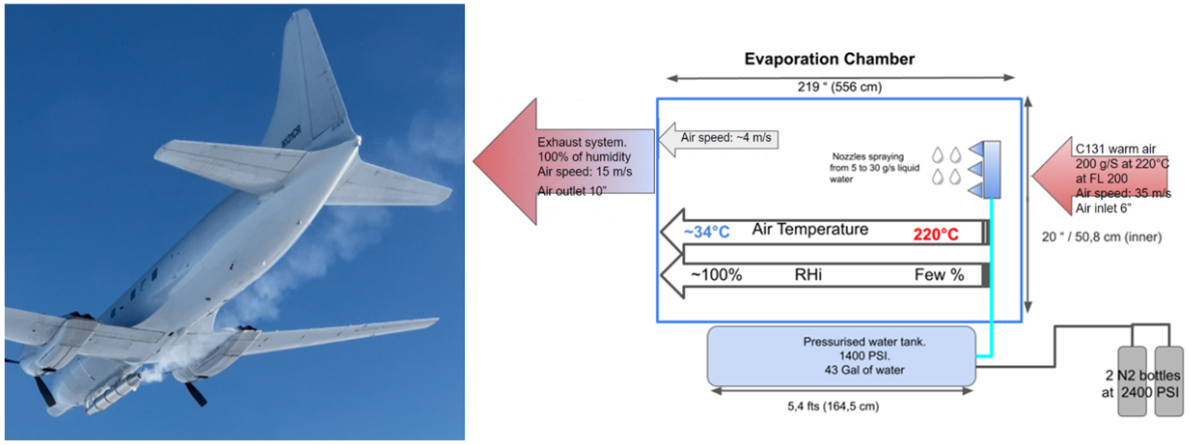

Figure 5. A picture of the evaporation chamber of the FCEE mounted to the fuselage of the C131 aircraft forming a contrail in flight is shown on the left and a schematic of the FCEE on the right (pictures courtesy of Airbus).

the seasonal and vertical evolution of these frequencies. These studies resulted in Minneapolis, USA, in December 2023 being selected to conduct the campaign (Mackay et al., 2025).

During the Nephele flight test campaign, NOAA GFS (Global Forecast System) forecasts were used for flight planning to predict ISSRs and areas of potential persistent contrails. GFS is a global model with a base horizontal resolution of 18 miles (28 km) between grid points and in the vertical, the model is divided into 127 vertical layers. It produces hourly forecast output for the first 120 hours. Taking into account the uncertainty of the forecast the criterion of ISSRs was relaxed to RHi > 90%. This resulted in larger contiguous ISSRs and simplified flight planning, while the probability of actually encountering ice supersaturated air masses without significant particle losses through sublimation remained within acceptable limits. To predict where persistent contrails would form, the ISSR was selected, where the ambient temperature was below 233 K, close to the homogeneous freezing limit.

Figure 6 shows the forecast of areas where persistent contrails may be formed (blue zones) and the temperature distribution with the RHi contours on 12 December 2023 at 15 h CST. The predicted central zone of ISSR is moving southeast over time; the flight plan, shown on the left (orange arrows), required the aircraft to leave the central point at 14 h CST and fly northwest to then intercept and fly through the blue zone, south eastwards, and then return to the departure point. The chase aircraft observed the FCEE producing a persistent contrail, which provided the ideal conditions for contrail measurements and monitoring of the atmospheric conditions.

At flight level 250 (∼400 hPa) the areas where persistent contrails can form evolve fast. The temporal and spatial resolution of the forecast is therefore very important to correctly predict areas of ice supersaturation and persistent contrail formation.

In-flight measurements of ambient conditions made on 12 December 2023 were later compared to the interpolated GFS forecast data, showing good agreement. A comparison to the ERA5 reanalysis data was also done, showing notable differences, highlighting the necessity of improvements in humidity forecasts (Mackay et al., 2025).

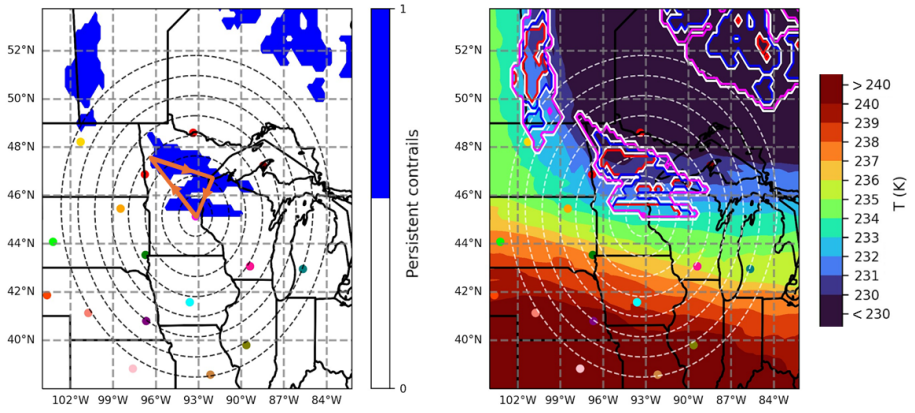

Figure 6. Prediction of persistent contrail areas (left) and the temperature distribution with RHi contours: red = 100%, blue = 90%, pink = 75% RHi (right) for 12th December for 15 h CST. The flight plan based on the persistent contrail predictions is shown in orange (left).

3.4 Setup of box model simulations

A Lagrangian Cloud Module (LCM) box model is used to investigate the microphysical evolution during contrail formation. The LCM employs a Lagrangian framework with a tracking of individual simulation particles, representing a certain number of real aerosol particles and hydrometeors that share similar properties. This enables the evolution of particle properties by microphysical processes. These processes include hygroscopic growth and activation of solid particles into water droplets, condensational growth, homogeneous freezing of supercooled droplets, depositional ice crystal growth and accompanying latent heat release. The activation of particles into droplets is governed by the Kappa-Köhler equations (Petters and Kreidenweis, 2007). The growth of these droplets is calculated as described by Barrett and Clement (1988); Kulmala (1993). For the modeling of the homogeneous freezing, a combined approach is used (Bier et al., 2024), accounting for both the cooling rate (Riechers et al., 2013) and the water activity of the droplets (O and Wood, 2016). Depositional ice crystal growth is calculated according to the mass change of a single ice crystal described by Mason (1971). The LCM box model has been applied frequently in prior studies, including Bier et al. (2022) for kerosene as well as Bier et al. (2024) and Zink et al. (2026) for hydrogen combustion. It is used in Hillenbrand and Unterstrasser (2026) to investigate contrail formation from fuel cell exhaust including droplet formation via homogeneous droplet nucleation (HDN). While previous studies have employed a multiple trajectory sampling of the aircraft plume, Bier et al. (2022) also demonstrated that the mean trajectory approach yields results in close agreement with ensemble simulations.

The simulation results help to better understand the effects observed during the measurements. For example, they provide information about the evolution of the supersaturation shortly behind the exhaust plane of the FCEE (Fig. 9 c). And by gauging the timescale of the droplet and ice crystal formation process, the effect of the mixing of the different exhaust plumes can be estimated.

The model is fine tuned to the FCEE, by prescribing exhaust geometry, dilution, temperature, RH and aerosol number con-

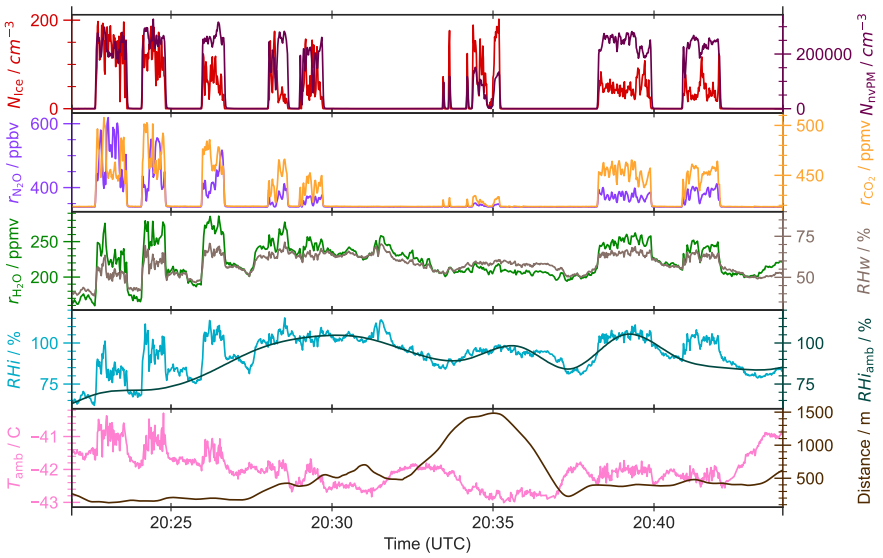

Figure 7. Timeseries of ice crystal (N_{Ice}) and non-volatile particle matter (N_{nvPM}) number concentrations, N_2O ($r_{\mathrm{N_2O}}$), CO_2 ($r_{\mathrm{CO_2}}$) and water vapor ($r_{\mathrm{H_2O}}$) mole fractions, $\mathrm{RH_w}$ and RHi, as well as the ambient RHi baseline ($\mathrm{RHi_{amb}}$), temperature (T_{Amb}) and the distance between lead and chaser aircraft measured during FT5 on the 12 December 2023 at 400 hPa.

centration. Measurement of the ambient conditions during the flight experiments are also taken into account for the simulation setup.

4 Results and discussion

In this section, data from three different flights, performed on the 3 December (Flight Test 2, or FT2), on 8 December (FT3) and 12 December (FT5) 2023, are analyzed. All sensors worked well throughout these three measurement flights. During FT2, the ambient temperature was between 228.5 to 230 K and RHi between 60 to 109% at 380 hPa. During FT3, the ambient temperature was around 242 K with low RHi of 10% at 410 hPa. During FT5 the ambient temperature ranged from 230 to 233 K and RHi from 30 to 105% at 400 hPa.

In Figure 7 an example time series of the collected data from a sampling sequence on the 12 December (FT5) is shown. During this flight the FCEE generated a contrail, but the C131's engines did not. The higher water vapor content and lower exhaust temperature in the FCEE led to a higher contrail threshold temperature T_{SAC} according to the Schmid-Appleman criterion (SAC) (Schumann, 1996).

4.1 Tracer analysis

We analyze the enhancement of both tracers over the ambient mole fractions ($\Delta r_{\mathrm{N_2O}}$ and $\Delta r_{\mathrm{CO_2}}$) derived from trace gas measurement data (as shown in the second column in Fig. 7). During the three analyzed flights enhancements above the background up to 700 ppbv for N_2O (at 20:11 UTC during FT5) and 160 ppmv for CO_2 (at 20:10 UTC during FT5) can be identified. The clear signal from the artificial dilution tracer above the background indicates, that the dimensioning of the emission source, as well as the time resolution and dynamic range of the instrument met the design goals for the ATReUS system. Minor adjustments to the N_2O flow rate, by increasing it to 9.33 slpm (90% of the maximum flow rate) were made for FT2 to FT5 in order to achieve a mean mole fraction of 815 ppmv at the FCEE exhaust plane and the $\Delta r_{\mathrm{N_2O}}$ shown in Fig. 9 (a).

The artificial dilution tracer enables a clear assignment of the measurements to the sampled exhaust gas plumes. More specifically, a high value for $\Delta r_{\mathrm{N_2O}}$ and a low value for $\Delta r_{\mathrm{CO_2}}$ at the same time indicate a sampling sequence of the FCEE, while a high $\Delta r_{\mathrm{CO_2}}$ with a simultaneous low $\Delta r_{\mathrm{N_2O}}$ indicates sampling of the C131 engine's exhaust. The maximum distance, where a N_2O signal was still detected was approximately 1.5 km.

Furthermore, different mixing regimes between the individual exhaust plumes can be distinguished. For very close measurements very high $\Delta r_{\mathrm{N_2O}}$ can be observed, while significantly lower $\Delta r_{\mathrm{CO_2}}$ were detected and vice versa. This indicates that the exhaust plumes are not uniformly mixed at this distance. For measurements at greater distances, the differences between $\Delta r_{\mathrm{N_2O}}$ and $\Delta r_{\mathrm{CO_2}}$ reduce, indicating a more homogeneous mixing. This qualitative observation is supported by analyzing the correlation coefficients of $\Delta r_{\mathrm{N_2O}}$ and $\Delta r_{\mathrm{CO_2}}$, shown in Fig. 8 (a). Increasing correlation coefficients indicate a more homogeneous mixing with increasing distance between lead and chaser aircraft. The exhaust plumes dilute according to a power law at the distances at which the measurements were taken. Dilution increases the plume diameter and leads to greater overlap between the plumes and a more homogeneous distributions of all tracers. At a distance of approximately 400 m, both tracers and thus also the plumes are well mixed.

During FT3, a proof-of-concept experiment was performed. In this experiment, the artificial dilution tracer was released in the immediate vicinity of the left engine exhaust of the lead aircraft (shown in Fig. 1 (b)). This was done for a total of 450 seconds and distances from 100 m to 600 m between the two aircraft. A second outlet for the artificial dilution tracer was installed close to the left hand engine's exhaust stack. The N_2O flow was redirected in flight and emitted through this outlet. As a result, CO_2 emitted from the engine and its dilution characteristics can be directly compared to that of the artificial dilution tracer. This provides the reference to verify the artificial dilution tracer release. The result of the experiment is shown in Fig. 8 (b). Here, $\Delta r_{\mathrm{N_2O}}$ is plotted over $\Delta r_{\mathrm{CO_2}}$ for all three flights (FT2, FT3 and FT5). The measurements during the proof-of-concept experiment are colored in orange and show a strong linear correlation (with a coefficient of determination of $R^2 = 0.884$) between the two tracers. This is an indication that both tracers dilute in a similar way. In the following analysis the data where the artificial dilution tracer was released close to the engine (instead of the FCEE) are not considered.

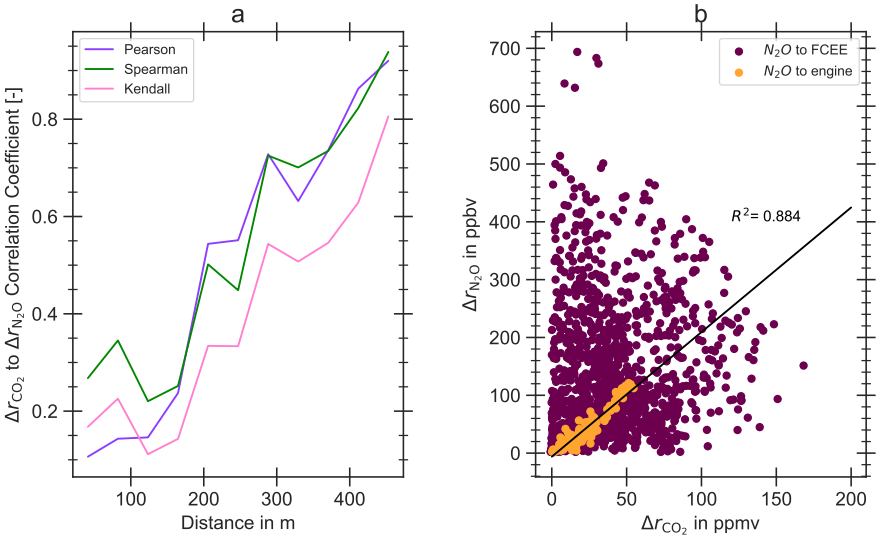

Figure 8. (a): Correlation coefficient between $\Delta r_{\mathrm{N_2O}}$ and $\Delta r_{\mathrm{CO_2}}$ over the distance between lead and chaser aircraft for combined data from FT2, FT3 and FT5. (b): Scattered $\Delta r_{\mathrm{N_2O}}$ and $\Delta r_{\mathrm{CO_2}}$ from the same flights are shown, colored depending on the N_2O outlet position. Data from the proof-of-concept experiment, during which N_2O was released close to the left engine, is shown in orange, with the linear regression line shown in black.

4.2 Exhaust dilution impact on maximum supersaturation

In this section we provide evidence of how the ATReUS system is able to quantify the dilution characteristic of an exhaust. We characterize the dilution of the FCEE, by comparing it to the dilution characteristic of the lead aircraft's engines, during measurement sequences, where the artificial dilution tracer was released directly inside the FCEE. This approach is shown in Fig. 9. Here the scattered $\Delta r_{\mathrm{N_2O}}$ over distance are shown in Fig. 9 (a) and $\Delta r_{\mathrm{CO_2}}$ in Fig. 9 (b). The color indicates the corresponding flight. In this case the dilution characterized by the $\Delta r_{\mathrm{CO_2}}$ represents the lead aircraft's engines, while $\Delta r_{\mathrm{N_2O}}$ quantifies that of the FCEE. A similar dilution behavior of CO_2 and N_2O is assumed here, as shown by the tracer positioning experiment mentioned in Section 4.1, where linear correlation between $\Delta r_{\mathrm{N_2O}}$ and $\Delta r_{\mathrm{CO_2}}$ was observed, when the artificial dilution tracer release is co-located with the engine. To better understand how fast the exhausts dilute we compare the $\Delta r_{\mathrm{N_2O}}$ emitted from the FCEE and $\Delta r_{\mathrm{CO_2}}$ emitted from the engines over the distance between lead and chaser aircraft. The radial distribution at each distance is represented in the variability of $\Delta r_{\mathrm{N_2O}}$ and $\Delta r_{\mathrm{CO_2}}$ and the dilution speed is indicated by the maximum values. These maxima correspond to a sampling of the respective plume center at a certain distance. A power-law fit similar to the one used in Schumann et al. (1998) is used, enabling a further comparison between the two exhaust types and past measurements.

Comparing the exponent of the power law fit gives an indication of the differences in dilution speed of the exhaust plumes. We find an exponent of 0.84 for the C131's piston engine and 1.23 for the FCEE. The former value is similar to the exponent of 0.9

proposed by Kärcher (1999) and 0.8 established by Schumann et al. (1998), based on measurements performed by the DLR research aircraft Dassault Falcon 20 (D-CMET) and NASA's Lockheed ER-2. In contrast the FCEE dilutes much faster, even faster than the parametrization by Zink and Unterstrasser (2026), used to model turbofan exhaust dilution, with an exponent of 1.15. Engine size scaling theory shows that the exponent depends on jet size and speed. An increase in jet size results in a decrease in dilution speed and an increase in jet speed results in an increase in dilution speed (Zink and Unterstrasser, 2026).

We calculate the maximum potential supersaturation that evolves due to the enhanced humidity in the plume of the FCEE, by performing two box-model simulation runs with the dilution adjusted to this analysis. One run takes the condensation of water vapor in the form of droplets and the resulting relaxation of local supersaturation into account (Fig. 9 c, pink graph). The second run does not take this process into account and thus corresponds to the maximum possible supersaturation without condensation (Fig. 9 c, green graph). The supersaturation is important due to its influence on droplet and subsequent ice crystal formation downstream of the exhaust plane. Contrails from kerosene-powered engines form on emitted soot particles, or additionally on volatile particle matter (vPM) in the low-soot regime (Ponsonby et al., 2025; Voigt et al., 2026). In contrast, contrails from hydrogen-based technologies lack soot as ice nuclei and the ice crystals therefore form on vPM or ambient aerosol. An increase in supersaturation can result in potential activation of additional nucleation cores or even different droplet formation pathways like HDN (Jansen and Heymsfield, 2015). This is particularly important for FC systems, which, due to their very humid and cooler exhaust gas (compared to conventional jet engines) and the lack of soot emissions, can reach supersaturation levels leading to HDN (Hillenbrand and Unterstrasser, 2026). In particular, validation of numerical models for these scenarios can only be done with the knowledge on the dilution characteristics (Lottermoser and Unterstrasser, 2025b).

One caveat of this tracer-based dilution speed assessment is the impact of exhaust location on the exhaust dilution characteristic. As the FCEE is mounted on the belly of the aircraft, while the engines are positioned at the wings, it is unclear in how far the positions of the exhausts may influence the individual exhaust plume dilution. This effect cannot be quantified here. Furthermore, the impact on the dilution associated with the swirl effect caused by a propeller, which would be used in a future FC system, cannot be replicated in the tested configuration.

4.3 Assessment of engine cross-contamination impact

The mixing of the exhaust plume of the FCEE with the exhaust of the Convair C131's engines, referred to here as cross-contamination, may affect the early contrail droplet formation by in-mixing of soot or other particles and water vapor. If the contrail formation from the FCEE has not been completed, cross-contamination can alter the ice crystal number and effective diameter by contributing nuclei for droplet formation. This in turn may lead to a change in the final contrail properties and therefore needs to be quantified. This effect is also particularly relevant for multi-fueled aircraft, or hybrid aircraft with a FC system.

First, the time scales for contrail formation has to be assessed. This can be done by calculating the temporal evolution of RHw in the plume. At a distance where the available humidity relaxes to sub-saturation, additional particles from the engines mixed into the FCEE plume cannot be activated any more. Model estimates indicate a distance of less than $12\,\mathrm{m}$ behind the FCEE (see pink graph in Fig. 9 c). Figure 5 (left) shows the contrail produced by the FCEE. A dense contrail already forms right

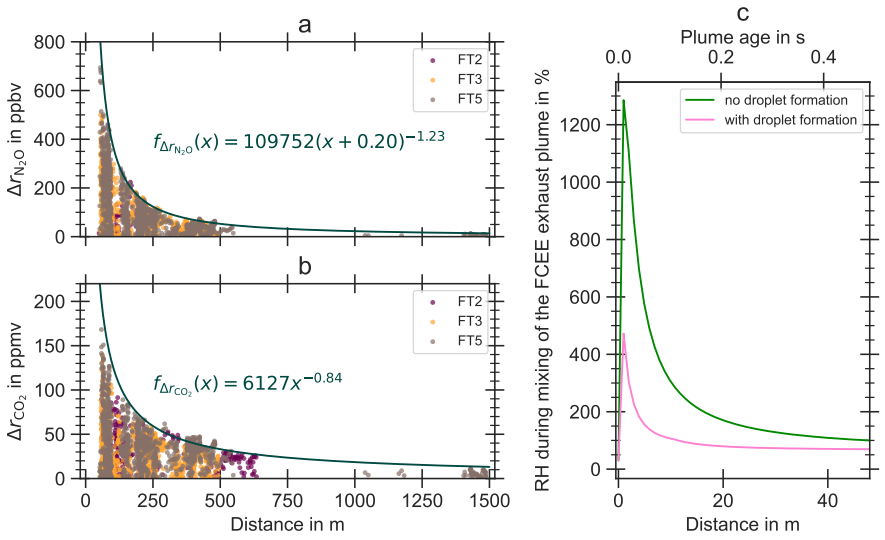

Figure 9. The panels on the left show Δr_{N_2O} (a) and Δr_{CO_2} (b) over the distance between release and sampling location. Panel a relates to the FCEE, panel b to the piston engine of the C131. Data points from FT2 are displayed in maroon, points from FT3 in orange and from FT5 in grey. For both species a dilution curve (dark green) was fitted to the data, conforming to the data points with the maximum Δr_{N_2O} and Δr_{CO_2} per respective distance. In panel c the evolution of RHw during isobaric mixing of the FCEE exhaust with ambient air is shown with droplet formation (pink) and without droplet formation (green).

behind (<0.5 m) the exhaust plane of the FCEE, illustrating the rapid dilution of the exhaust gases and subsequent relaxation of plume water saturation.

Further, the time and distance for mixing of the FCEE and the engine exhaust has to be derived. Using the artificial dilution tracer, cross-contamination effects can be assessed by comparing Δr_{N_2O} and Δr_{CO_2} for different sampling positions and mixing regimes. Here it is important to know at what distance downstream of the FCEE potential contaminant particles are mixed in (see Fig. 1 (a)). The measurements were taken at distances > 50 m. Here, mixing of the exhaust plumes has already occurred in all measurement sequences, yet with a range of concentrations. The ratios between Δr_{N_2O} and Δr_{CO_2} are used to categorize the distances ranges into an area of reduced cross-contamination and an area of significant cross-contamination.

By plotting the maximum Δr_{N_2O} and Δr_{CO_2} measured during the three flight tests in a grid separated by the distances between the two aircraft in the lateral (orthogonal to the flight direction) and longitudinal (in flight direction) directions the area of reduced cross-contamination was determined. Comparing these maxima, shown in Fig. 10, we find a difference in the distances of maximum Δr_{N_2O} and Δr_{CO_2}. Maximum Δr_{N_2O} was measured at distances between 53 to 57 m, while maximum Δr_{CO_2} was measured at distances between 58 to 62 m. This indicates that the mixing of the plumes is at an early state for distances closer than 58 m (marked by the red line in Fig. 10). Therefore for distances closer than 58 m reduced cross-contamination is expected.

By looking at video footage of FT2, a visual inspection of the contrail mixing distances provided comparable results and thus

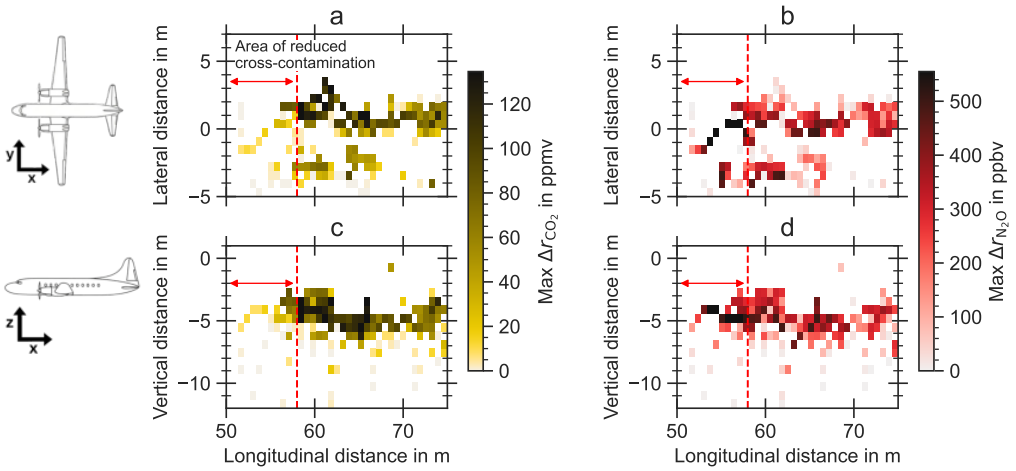

Figure 10. Spatial distribution of measurements from FT2, FT3 and FT5 in the x-y plane (a) and (b) and the x-z plane (c) and (d). x is the axis in flight direction or longitudinal distance, y the lateral distance (orthogonal to flight direction) and z is the vertical (altitude) difference. The grid cells are color coded by max Δr_{CO_2} (a) and (c) and correspondingly for max Δr_{N_2O} (b) and (d). The dotted red line separates the areas of the maximum Δr_{N_2O} ($x < 58m$) and maximum Δr_{CO_2} ($x > 58m$) measurements. The aircraft schematics shown here are not to scale.

support the tracer analysis.

Looking at the estimated distance, where the FCEE exhaust plume is sub-saturated again (<12 m) and the established area of reduced cross-contamination (50 to 58 m), we conclude that the consequent mixing of exhaust particles and gases from the C131's engines into the plume of the FCEE likely takes place significantly after the water supersaturation has relaxed to below 100% and therefore does not effect the number of contrail ice particles.

4.4 Microphysical properties of contrails formed behind the FCEE

In the next two sections, we show that the artificial dilution tracer can be used to calculate dilution-corrected emission metrics, like AEI_{ice} of the FCEE (Section 2.4). Data from FT5 (see Fig. 7) is used here. During the flights, the FCEE was supplied by unfiltered air taken near the main engines. The number concentrations of total particulate matter (tPM) inside the FCEE air supply duct was measured during a later flight and provided concentrations greater than $3 \cdot 10^6\,\mathrm{cm}^{-3}$ (due to saturation effects of the instrumentation, this represents only a lower limit of the particle contamination). Thus, the measurements are not representative for fuel cell exhaust conditions where it is expected to have particle-free emissions. The FCEE contrail ice particles formed on exhaust particles of similar concentrations as in conventional exhaust, yet with higher water vapor emissions and lower exhaust temperatures.

During FT5, a measurement sequence was recorded in which the lead and chase aircraft flew at 400 hPa in an air mass at temperatures slightly below 235 K and RHi above 70%. According to theory, the onset of contrail droplet formation for higher water vapor emissions and lower exhaust temperatures occurs at higher ambient temperatures than the onset of droplets

formed behind conventional aircraft. For these conditions we investigate the microphysical properties of the contrail. In this temperature range, the higher contrail formation threshold temperature T_{SAC} of the FCEE ensures that all measured ice crystals were produced by the FCEE, because the engines of the C131 did not produce a contrail.

Fig. 11 (a+b) shows the varying optical properties of the contrail produced by the FCEE in two different air masses. Throughout the measurement, the FCEE was kept at an exhaust RHw of 34 to 39% and an exhaust temperature of 320 to 322 K. For this flight segment, the optical properties of the early contrail (observed from the point of view of the C131) changed. The thin contrail with low particle number concentrations (Fig. 11 a) evolved to an optically thick contrail with high number concentrations and thus a higher $\mathrm{AEI_{ice}}$ value (Fig. 11 b). The thin contrail (Fig. 11 a) developed at low ambient RHi of 44% at 232 K and was not persistent. $\mathrm{AEI_{ice}}$ was assessed to be $4.2 \cdot 10^{13}\,\mathrm{kg}^{-1}$ with a MVD of 1.9 to 2.8 µm (this sequence is not shown in Fig. 7). The optically thick contrail (Fig. 11 b) on the other hand corresponds to a significantly higher $\mathrm{AEI_{ice}}$ of $3.8 \cdot 10^{15}\,\mathrm{kg}^{-1}$ with a MVD of 4 to 4.1 µm. The contrail in this case was persistent at ambient RHi of 103% at an ambient temperature of 230.5 K.

Here, we calculate $\mathrm{AEI_{ice}}$ based on a reference mass flow, connected to the operating conditions of the FCEE. In this case a hypothetical hydrogen fuel flow, calculated from stoichiometric conversion of hydrogen to water, corresponding to the water vapor mass flow from the FCEE, was used as the reference. $\mathrm{AEI_{ice}}$ derived in this way helps to compare exhaust and contrail properties to those from conventional engines, where $\mathrm{AEI_{ice}}$ is calculated using the established method with CO_2 as the tracer. During FT2, contrails formed behind the FCEE but also behind the engines of the C131 (see Fig. 11 c). The mission profile included a climb to 380 hPa. During the climb the chaser aircraft stayed close to the C131 to observe the onset of the contrails. At first the FCEE formed a contrail, which started out very faint and became optically denser during ascent, but remained non persistent during this section of the flight. The aircraft then entered a region of low ambient temperature (228.5 K) and high humidity (>100% RHi) where the C131's engines started generating a contrail too and the contrails became persistent (see Fig. 11 c). Due to fast mixing of ice crystals from the three contrails, we did not analyze this data, but found that there is only a narrow range within which persistent contrails are formed exclusively by the FCEE and not also by the aircraft's engines. This is relevant also for contrail climate models which estimate the formation in comparison to regional turbo prop aircraft. Due to the very high T_{SAC} of fuel cell systems (Gierens, 2021) (and of the FCEE) droplet formation occurs almost always, thus droplet freezing or contrail persistence become the limiting factors for contrails (Megill and Grewe, 2025).

4.5 Ambient temperature-dependent $\mathrm{AEI_{ice}}$ and freezing fraction

We investigate the impact of the temperature difference ΔT_{hf} between the homogeneous freezing temperature T_{hf} = 235.15 K and the ambient temperature T_{amb} on the formation of ice crystals, $\mathrm{AEI_{ice}}$ and the freezing fraction of droplets formed behind the FCEE. (As a simplification, T_{hf} is assumed to be constant here, the actual homogeneous freezing temperature of a droplet is dependent on its particle properties (O and Wood, 2016).) To do this we need to disentangle the impact of the FCEE exhaust conditions on the contrail. The 1 Hz-resolved mixing line slope G of the FCEE is calculated based on the exhaust and ambient conditions at the time of the contrail measurement ($G = (e_{\mathrm{exhaust}} - e_{\mathrm{amb}})/(T_{\mathrm{exhaust}} - T_{\mathrm{amb}})$) according to Schumann (1996). In addition to being used to calculate T_{SAC}, G is also suitable for detecting changes in the combined temperature and humidity

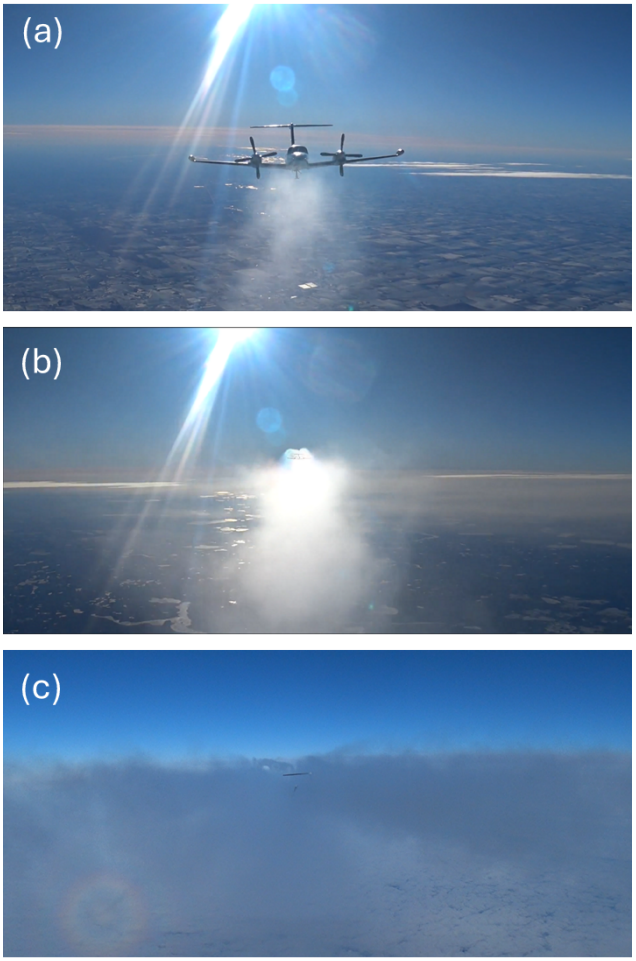

Figure 11. Pictures of the contrail evolution from the perspective of the FCEE aboard the C131, with similar FCEE exhaust conditions but different ambient temperature and humidity conditions. The chaser aircraft is visible while sampling. (a) Optically thin non-persistent contrail ($AEI_{ice} = 4.2 \cdot 10^{13}\,\mathrm{kg}_{\mathrm{hydrogen}}^{-1}$ with a MVD of 1.9 to 2.8 µm) at low ambient RHi of 44% and 232 K (FT5). (b) Optically thick persistent contrail ($AEI_{ice} = 3.8 \cdot 10^{15}\,\mathrm{kg}_{\mathrm{hydrogen}}^{-1}$ with a MVD of 4 to 4.1 µm) at high ambient RHi of 103% and 230.5 K (FT5). (c) Three persistent contrails at high ambient RHi of 109% and 228 K (FT2): two contrails evolve from the engines of the C131, one from the FCEE.

conditions at the outlet of the FCEE. An increase in water vapor emission or a decrease in exhaust temperature is reflected in an increase in G. Consequently, G is very high for the FCEE, compared to conventional aircraft engines. Due to the high G value, T_{SAC} is also high (260 to 275 K). Therefore droplet formation always occurs in the encountered conditions. For the data shown here T_{amb} ranges from 230.2 to 231.8 K and ΔT_{hf} from -3.3 to -5 K. The FCEE provided similar exhaust conditions ($44\,\mathrm{Pa\,K^{-1}} < \mathrm{G} < 57\,\mathrm{Pa\,K^{-1}}$) throughout the entire measurement sequence. The change in the mixing line slope G is indicated by the color code in Fig. 12 (c) and was mainly due to variations in the exhaust gas temperature. Given the high G and the associated small relative changes of G, we assume that these variations in the exhaust conditions do not have an influence on

the mechanism of ice crystal formation.

At low ΔT_{hf} ($\sim 3\,\mathrm{K}$), droplets are initially formed and grow in size. Due to the fast dilution shortly behind the exhaust plane (see Fig. 9), these newly formed droplets are entrained quickly (< $0.2\,\mathrm{s}$) into air sub-saturated with respect to water. Only a fraction of these droplets (mainly the larger ones) can survive until they finally freeze. At temperatures above 231 K only a small fraction (< 10%) of droplets freeze. We provide the fraction of frozen droplets (number of ice crystals measured divided by the max number of ice crystals) assuming that at the lowest ambient temperatures (highest ΔT_{hf}) contrail formation was complete and the maximum number of ice crystals was produced (see Fig. 12 c). With decreasing ambient temperature, thus decreasing ΔT_{hf}, the survival fraction of ice crystals increases almost instantaneously within a narrow temperature range between 231.5 and 229.5 K. With lower temperatures, mean $\mathrm{AEI_{ice}}$ (black diamonds in Fig. 12) increase by one order of magnitude while the effective diameter decreases drastically from $5.2\,\mu\mathrm{m}$ to $3.2\,\mu\mathrm{m}$ (color-coded in Fig. 12 a). Due to conservation of water, the excess water vapor (water vapor above the saturation threshold available for condensation) condenses on existing particles. As the ice crystal number increases, the available excess water vapor per ice crystal consequently decreases which is reflected in the decreasing MVD. RHi, shown as color code in Fig. 12 (b), here represents the in-plume measurements. In the first part of the flight segment, at higher temperatures ($231\,\mathrm{K} < T_{\mathrm{amb}} < 232\,\mathrm{K}$), RHi is low (< 90%), thus the available water vapor for condensation is low, reflected in a small MVD of the ice crystals. $\mathrm{AEI_{ice}}$ is mainly influenced by ΔT_{hf}, while RHi plays a stronger role for the survival of the particles rather than the formation. In contrast, the size of the ice crystals is influenced by both the number of ice crystals and RHi, leading to low $\mathrm{AEI_{ice}}$ and small MVD in the higher temperature range between 231 K $< T_{\mathrm{amb}} <$ 232 K.

We discuss the behavior of $\mathrm{AEI_{ice}}$ near the contrail limit temperature for the FCEE in light of previous measurements of contrail $\mathrm{AEI_{ice}}$ from current kerosene engines. Bräuer et al. (2021) provided first experimental data on the temperature dependence of $\mathrm{AEI_{ice}}$ near $\mathrm{T_{SAC}}$. The limited data in the region of -5 K< ΔT_{SAC}< 0 K showed an increase of the activation fraction (number of soot particles that form ice crystals) of 14% slightly above 0 K to 100% at -5 K below $\mathrm{T_{SAC}}$. In the region near $\mathrm{T_{SAC}}$, $\mathrm{AEI_{ice}}$ is particularly sensitive to the ambient temperature (Kärcher et al., 2015). For the FCEE, we find a similar behavior, but related to ΔT_{hf} not ΔT_{SAC}. An increase in $\mathrm{AEI_{ice}}$ by at least one order of magnitude and a decrease in ice particle size by half in a temperature interval of only 1 K was observed. This is qualitatively in-line with current model calculations (see Section 3.4). For a quantitative assessment we note that the slope of the temperature-dependent $\mathrm{AEI_{ice}}$ depends on various parameters ($\mathrm{EI_{H_2O}}$, exhaust temperature and aerosol number concentration, dilution speed etc.) and requires precise knowledge of all parameters to achieve sufficient agreement with models.

Aircraft propelled by fuel cells will most likely fly at lower altitudes compared to current aircraft. Ambient temperatures will be higher at the lower flight levels and contrail formation from conventional kerosene combustion reduced (Gierens, 2021; Kaufmann et al., 2024). For fuel cell systems with high water vapor and low temperature exhaust composition the criterion for droplet formation is fulfilled almost everywhere. However, contrail ice crystal formation depends mainly on ambient temperature which affects the freezing of the droplets (Megill and Grewe, 2025). We here provide a contrail case near the homogeneous freezing temperature threshold and observe a large variability in dilution-corrected contrail ice number and size. The MVD of ice crystal size distribution (2 to 6 µm) measured here is for the fully frozen contrails slightly larger than has

been observed for conventional contrails at a larger plume age (1-2 min). In particular Voigt et al. (2021) show effective contrail ice crystal diameters of 1.9 $\mu\mathrm{m}$ for Jet A1 fuel and 2.7 $\mu\mathrm{m}$ for low-aromatic semisynthetic jet fuel. Thus comparison to those data is limited given that particle growth in the first minute is mainly modulated by ambient humidity. The larger ice crystals in the early FCEE plume result from the higher water vapor emissions of the FCEE but also from higher amounts of available water vapor in the ambient atmosphere at this flight level (400 hPa). These "high-ambient-temperature" contrails have not been measured before and the measurement data can be used to validate models simulating cold and humid exhausts. Although the exhaust conditions may not necessarily represent relevant fuel cell exhaust conditions in the future, the data provide a basis to study contrails formed at higher ambient temperatures and near-threshold conditions.

4.6 Comparison of box model simulations to in-flight data

Here, the AEI values calculated from the LCM box model simulations are compared to the values derived from the measurements. For this, the initial model parameter are adjusted to fit the experiment in terms of FCEE and ambient conditions. The function $f_{\Delta \mathrm{rN_2O}}(x)$ given in Fig. 9 (a) is prescribed as the representative mean dilution of the aircraft plume for our simulations. Given the small velocity of the exhaust compared to the aircraft velocity ($v_{\mathrm{ac}} \approx 100\,\mathrm{m/s}$), the dilution function $f_{\Delta \mathrm{rN_2O}}(x)$ is transformed into a temporal evolution via v_{ac}. The expansion of the plume as well as the change in temperature and humidity inside the plume is then calculated based on this prescribed dilution function. The low exhaust velocity and the small exhaust area both lead to a rapid initial dilution of the plume, requiring a fine temporal resolution to accurately resolve the early mixing and cooling phases. To account for these effects we use a timestep $\Delta t_{\mathrm{LCM}} = 10^{-4}\,\mathrm{s}$ in all simulations. A range of exhaust temperature and humidity conditions that are representative for thermodynamic exhaust conditions during the measurements are set. A constant ambient pressure $p_{\mathrm{amb}} = 400\,\mathrm{hPa}$ and an ice-saturated atmosphere ($\mathrm{RH_{i,amb}} = 100\,\%$) is assumed, with ambient temperatures varied between $230\,\mathrm{K}$ and $233\,\mathrm{K}$.

Due to the experimental setup of the FCEE flown during the Nephele flight test campaign, its exhaust inadvertently contained a large number of particles. The source of the particles is unknown, but model simulations suggest that small traces of oil can have a big impact on the particle number concentration in the plume (Zink et al., 2025). As the exact number concentration of these particles remains uncertain, we conduct simulations for two representative values $n_{\mathrm{exh}} = \left\{10^7, 10^8\right\}\,\mathrm{cm^{-3}}$, spanning the likely range of exhaust particle concentrations in the FCEE exhaust during the measurements.

$\mathrm{AEI_{ice}}$ values calculated from the simulations are shown in Figure 12 (d). The simulations show a strong dependence of the number of ice crystals on the ambient temperature, for ambient temperatures close to T_{hf}. As mentioned above, for the in-flight data we assume T_{hf} to be 235.15 K, but in reality and also in the model we use T_{hf} expression that depends on particle size and solubility. A strong decrease in $\mathrm{AEI_{ice}}$ is observed with increasing ΔT_{hf}. During the early plume stage the exhaust is highly supersaturated with respect to water, which leads to droplet activation of all emitted aerosols. This is in contrast to conventional aircraft where the activation is limited by the supersaturation in the plume. For ambient temperatures close to T_{hf}, only a fraction of these droplets freeze and subsequently survive in the sub-saturated (with respect to water) atmosphere ($\mathrm{RH_{w,amb}} < 100\,\%$ and $\mathrm{RH_{i,amb}} = 100\,\%$). The simulations also show a strong dependence on the ambient temperature where the $\mathrm{AEI_{ice}}$ starts to decrease, as well as the magnitude of the decrease on the number concentration of the emitted aerosols.

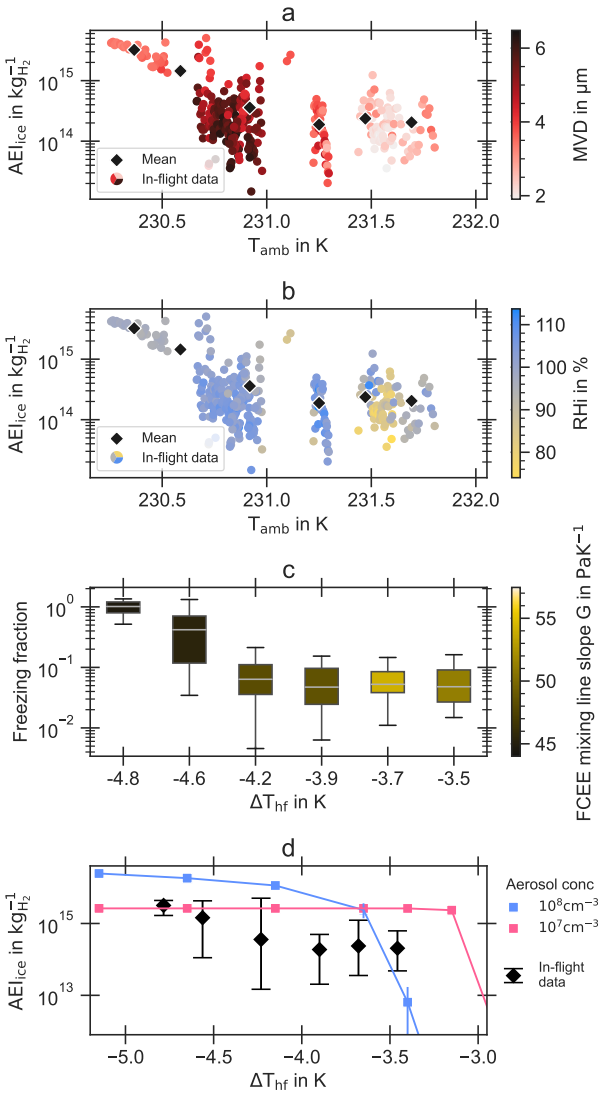

Figure 12. In panel a AEI_{ice} values from FT5 are plotted over the ambient temperature color-coded with the mean volume diameter (MVD) of the ice crystals. Mean AEI_{ice} values are displayed as black diamonds. Panel b shows the same plot, but color-coded with the in-plume RHi. Panel c shows the freezing fraction of ice particles over the temperature difference to T_{hf} color-coded with the mixing line slope G (Schumann, 1996) of the FCEE. Box model simulation results are displayed in panel d, assuming varying aerosol concentrations of $10^7\ \mathrm{cm}^{-3}$ (pink) and $10^8\ \mathrm{cm}^{-3}$ (blue) in the FCEE exhaust. The measured AEI_{ice} values are displayed in black.

While we assume that during the measurements, the aerosol load in the FCEE plume remains constant, we explore the dependence of particle number on the AEI_{ice} evolution with temperature with the model. For cases with more aerosol particles emitted by the FCEE and a therefore higher number of condensation nuclei, the available excess water vapor is distributed

across more droplets which subsequently are smaller. The lower freezing temperatures of small droplets results in a lower freezing fraction of these droplets close to T_{hf}.

To gauge the impact of the mixing line slope on the ice crystal formation, the exhaust conditions assumed for the FCEE in the model were also varied (exhaust temperature between 40 to 55 °C, with RH ranging from 60 to 30%). For cases where none of the droplets evaporate before they freeze, the FCEE exhaust conditions have no significant effect on $\mathrm{AEI_{ice}}$. In cases where only a fraction of droplets freeze the mixing line slope does affect $\mathrm{AEI_{ice}}$, because an increased water vapor amount in the exhaust leads to larger droplets on average. Therefore, more droplets can freeze before they evaporate, leading to higher $\mathrm{AEI_{ice}}$ for moister exhaust conditions (the exhaust dependent effect on $\mathrm{AEI_{ice}}$ is visualized by the vertical colored lines in Fig. 12d). Both the data from the simulations and the in-flight measurements show that the number of ice crystals formed at ambient temperatures near the homogeneous freezing temperature is limited by the freezing process of the droplets. The ambient temperature where $\mathrm{AEI_{ice}}$ starts to strongly decrease, as well as the magnitude of this decrease differ between model and experiment. However, given the uncertainties in both the model and experiment, it is difficult to pinpoint clear reasons for this discrepancy. One reason is the uncertainty of temperature measurement of $\pm$ 1°C. Another model-related aspect is the limitation of the results to the plume center line (Lewellen, 2020). The strength of the comparison is that both methods show the relevance of the freezing process in a similar temperature range. The model simulations also support the assumption that no HDN took place during the flights, as the activation of the emitted particles led to a subsequent depletion of available water vapor, before the high supersaturation required for HDN was reached.

5 Conclusions

In this work the contrail of a prototype fuel cell exhaust emulator (FCEE) was characterized as part of the Nephele flight test campaign. The setup of the FCEE aboard a Convair C131 and first FCEE contrail measurements in ambient conditions near the homogeneous freezing temperature aboard a Piper Cheyenne 400LS chaser aircraft with a large suite of instruments is described.

An artificial dilution tracer release and sampling system called ATReUS was designed, deployed and tested during the test flights. N_2O proved to be a suitable trace gas for this system. We provide an overview of three flights and the dilution properties of both the C131's engine exhausts using the engine emission tracer CO_2 and the FCEE emitting the artificial dilution tracer N_2O. Furthermore, cross-contamination effects from the engines are assessed, by analyzing the spatial distribution of both tracers. We demonstrate the possibility to calculate dilution-corrected emission and contrail metrics, such as $\mathrm{AEI_{ice}}$, using the artificial dilution tracer.

The setup of the ATReUS system worked well throughout the test flights and fulfills the requirements set in advance for the system. The use of the artificial dilution tracer allowed for a clear identification of exhaust plumes, which is particularly useful in cases where multiple emission sources are present, and in case of a hydrogen propulsion system, where no CO_2 is emitted. Measuring the plume mixing and dilution effects of the exhaust with ambient air is of key importance to understand contrail formation processes from fuel cell systems and to establish comparability between aircraft types and operational states.

The calculated AEI_{ice} values demonstrate the capability of the novel artificial tracer system to enable the assessment of dilution-corrected emission metrics from in-flight measurements. For similar exhaust conditions of the FCEE, with high water vapor emissions and low exhaust temperatures with large mixing line slopes $G > 44\,\mathrm{Pa\,K^{-1}}$, we provide measurements of contrail properties at temperatures near the homogeneous freezing threshold. A large influence of the difference between ambient and threshold temperature on AEI_{ice}, MVD and freezing fraction of the ice crystals was observed. With increasing ΔT_{hf} (higher ambient temperatures), AEI_{ice} decreases by more than one order of magnitude while the MVD increases. Close to the freezing threshold, droplets which are entrained into air sub-saturated with respect to water evaporate shortly after formation. At high ΔT_{hf}, these droplets freeze before they can evaporate and survive in air saturated with respect to ice. Higher AEI_{ice} are anti-correlated with lower MVD as expected from mass conservation.

Despite the fact, that the FCEE did not provide relevant clean conditions to explore low emission aircraft exhaust conditions we show that in principal the humid and cold conditions can be emulated. We recommend future tests with similar experimental setups, but in which particle contamination of the emulated exhaust is avoided, to explore mitigation options of contrails from fuel cell exhaust.

Code and data availability. The data is provided in the HALO database at https://halo-db.pa.op.dlr.de/mission/144. Free primary data access begins on 30 April 2030. Until then, download access and access to further data will be given upon request by the mission PI.

Video supplement. To access captured video from the Nephele flight test campaign, contact the Author.

Appendix A: Laboratory characterization of the Li-7820 N_2O trace gas analyzer

The Nephele flight test campaign in December 2023 was the first deployment of the Li-7820 N_2O/H_2O gas analyzer on an aircraft by the DLR. In order to guarantee safe and reliable operation, the instrument was modified and extensively tested in the laboratory in its modified state. The main modification is the implementation of a more powerful pump to enable operation in a lower pressure environment. The instrument is operated in a pressurized cabin, therefore no major modifications to the instrument housing are necessary. Reference gas measurements using stable N_2O mole fractions were performed with and without the modifications to ensure no distortion of data quality were induced. Measurements with and without the new pump, a Agilent IDP-3 dry scroll pump, were carried out, with no notable influence on the measurement being detected. The modified setup was tested at different inlet pressures to ensure functionality at the required sampling altitudes during the measurement flights. The minimal inlet pressure of the setup was assessed as well, with the measurements remaining stable down to approximately 250 hPa, corresponding to a maximum measurement altitude of 10000 m or FL340 MSL. Two long-term measurements were done to assess instrument drift, thereby identified as < 0.1 ppbv per hour of continuous measurement. The instrument precision (1σ) was determined to be 0.1 ppbv for 1 Hz measurements and 0.05 ppbv applying 5 s averaging under laboratory conditions. To ensure a good measurement accuracy and to compensate for instrument drift it was decided to use the calibration strategy described in Appendix B. The instrument in its modified state is well suited for airborne measurements.

Appendix B: Calibration strategy of the trace gas instrumentation

To ensure comparability to other instruments and data sets and compensate for instrument drift all trace gas measurements must be referenced to an international standard. During the Nephele flight test campaign this was done by performing two-point calibrations for both the Li7000 and Li7820. To do this a secondary low and a high gas standard were measured, before and after each flight in case of the N_2O sensor and during the flights before and after a chase sequence in case of the CO_2 sensor. We note here that this calibration strategy is sufficient in this case, as only the enhancement of the trace gases above the ambient mole fraction are used for the analysis, which reduces the accuracy requirements for both instruments. All secondary standards used during the Nephele flight test campaign were referenced beforehand in the laboratory in Oberpfaffenhofen to primary low and high standards each. These were provided by the National Oceanic and Atmospheric Administration (NOAA) Global Monitoring Laboratory (GML) (Kitzis, 2017). As GML is participating in the Global Atmospheric Watch Program of the World Meteorological Organization these gases ensure international comparability. The procedure for the two-point calibrations is described in equations B1-B3, a linear fit function is applied to all measured mole fractions:

$$x_{\mathrm{cal}} = m \cdot x_{\mathrm{meas}} + t \tag{B1}$$

Here, x_{cal} and x_{meas} are the calibrated and measured mole fractions respectively. m is the slope and t the intercept of the fit function. They are calculated as follows:

$$m = \frac{H_{\mathrm{true}} - L_{\mathrm{true}}}{H_{\mathrm{meas}} - L_{\mathrm{meas}}} \tag{B2}$$

$$t = L_{\mathrm{true}} - m \cdot L_{\mathrm{meas}} \tag{B3}$$

Here the true high (H_{true}) and low (L_{true}) mole fractions of the standards are related to the measured high (H_{meas}) and low (L_{meas}) values. For the flight data m and t are interpolated over the whole flight when multiple standard measurements are available. The correction was applied post-flight on all data used for the analysis presented here.

Author contributions. Coordination and planning of the project: T.J., J.C. and C.R.; Provision, operation and piloting of the aircraft: A.V and R.V.; FCEE system design: J.C. and F.T.; Operation, installation and design of the scientific instrumentation: S.B., M.P., A.M., D.S., G.N., E.C., V.H., M-L., P.S., C.H. and T.J.; Conceptualization: S.B. and T.J.; Methodology, investigation and visualization: S.B.; Original draft: S.B.

Competing interests. J.C., F.T., C.M., F.L. and C.R. are employed by Airbus Operations. R.V. and A.V. are employed by AV Experts LLC. All the other authors declare that they have no conflict of interest.

Acknowledgements. The author thanks Airbus for the FCEE system design, for funding the flights and for working on a more sustainable future of aviation. Thanks to Airbus and AV Experts for making the project possible. SB, GN, DH thank the DLR project H2CONTRAIL for their funding. COMPANION, grant agreement ID 101140627.

References

Airbus: Global Market Forecast, https://www.airbus.com/en/products-services/commercial-aircraft/global-market-forecast, [Accessed: 2026-11-10 10:13:30], 2026.

Barrett, J. and Clement, C.: Growth rates for liquid drops, Journal of Aerosol Science, 19, 223–242, https://doi.org/10.1016/0021-8502(88)90225-X, 1988.

Bickel, M., Ponater, M., Burkhardt, U., Righi, M., Hendricks, J., and Jöckel, P.: Contrail Cirrus Climate Impact: From Radiative Forcing to Surface Temperature Change, Journal of Climate, 38, 1895–1912, https://doi.org/10.1175/JCLI-D-24-0245.1, 2025.

Bier, A., Unterstrasser, S., and Vancassel, X.: Box model trajectory studies of contrail formation using a particle-based cloud microphysics scheme, Atmospheric Chemistry and Physics, 22, 823–845, https://doi.org/10.5194/acp-22-823-2022, 2022.

Bier, A., Unterstrasser, S., Zink, J., Hillenbrand, D., Jurkat-Witschas, T., and Lottermoser, A.: Contrail formation on ambient aerosol particles for aircraft with hydrogen combustion: a box model trajectory study, Atmospheric Chemistry and Physics, 24, 2319–2344, https://doi.org/10.5194/acp-24-2319-2024, 2024.

Boeing: Commercial Market Outlook, https://www.boeing.com/commercial/market/commercial-market-outlook, [Accessed: 2026-11-10 10:15:34], 2026.

Borella, A., Boucher, O., Shine, K. P., Stettler, M., Tanaka, K., Teoh, R., and Bellouin, N.: The importance of an informed choice of CO_2-equivalence metrics for contrail avoidance, Atmospheric Chemistry and Physics, 24, 9401–9417, https://doi.org/10.5194/acp-24-9401-2024, 2024.

Bräuer, T., Voigt, C., Sauer, D., Kaufmann, S., Hahn, V., Scheibe, M., Schlager, H., Diskin, G. S., Nowak, J. B., DiGangi, J. P., Huber, F., Moore, R. H., and Anderson, B. E.: Airborne Measurements of Contrail Ice Properties—Dependence on Temperature and Humidity, Geophysical Research Letters, 48, e2020GL092 166, https://doi.org/10.1029/2020GL092166, 2021.

Burkhardt, U., Bock, L., and Bier, A.: Mitigating the contrail cirrus climate impact by reducing aircraft soot number emissions, npj Climate and Atmospheric Science, 1, 37, https://doi.org/10.1038/s41612-018-0046-4, 2018.

Calvin, K., Dasgupta, D., Krinner, G., Mukherji, A., Thorne, P. W., Trisos, C., Romero, J., Aldunce, P., Barrett, K., Blanco, G., Cheung, W. W., Connors, S., Denton, F., Diongue-Niang, A., Dodman, D., Garschagen, M., Geden, O., Hayward, B., Jones, C., Jotzo, F., Krug, T., Lasco, R., Lee, Y.-Y., Masson-Delmotte, V., Meinshausen, M., Mintenbeck, K., Mokssit, A., Otto, F. E., Pathak, M., Pirani, A., Poloczanska, E., Pörtner, H.-O., Revi, A., Roberts, D. C., Roy, J., Ruane, A. C., Skea, J., Shukla, P. R., Slade, R., Slangen, A., Sokona, Y., Sörensson, A. A., Tignor, M., Van Vuuren, D., Wei, Y.-M., Winkler, H., Zhai, P., Zommers, Z., Hourcade, J.-C., Johnson, F. X., Pachauri, S., Simpson, N. P., Singh, C., Thomas, A., Totin, E., Arias, P., Bustamante, M., Elgizouli, I., Flato, G., Howden, M., Méndez-Vallejo, C., Pereira, J. J., Pichs-Madruga, R., Rose, S. K., Saheb, Y., Sánchez Rodríguez, R., Ürge Vorsatz, D., Xiao, C., Yassaa, N., Alegría, A., Armour, K., Bednar-Friedl, B., Blok, K., Cissé, G., Dentener, F., Eriksen, S., Fischer, E., Garner, G., Guivarch, C., Haasnoot, M., Hansen, G., Hauser, M., Hawkins, E., Hermans, T., Kopp, R., Leprince-Ringuet, N., Lewis, J., Ley, D., Ludden, C., Niamir, L., Nicholls, Z., Some, S., Szopa, S., Trewin, B., Van Der Wijst, K.-I., Winter, G., Witting, M., Birt, A., Ha, M., Romero, J., Kim, J., Haites, E. F., Jung, Y., Stavins, R., Birt, A., Ha, M., Orendain, D. J. A., Ignon, L., Park, S., Park, Y., Reisinger, A., Cammaramo, D., Fischlin, A., Fuglestvedt, J. S., Hansen, G., Ludden, C., Masson-Delmotte, V., Matthews, J. R., Mintenbeck, K., Pirani, A., Poloczanska, E., Leprince-Ringuet, N., and Péan, C.: IPCC, 2023: Climate Change 2023: Synthesis Report. Contribution of Working Groups I, II and III to the Sixth Assessment Report of the Intergovernmental Panel on Climate Change [Core Writing Team, H. Lee and J. Romero (eds.)]. IPCC, Geneva, Switzerland., Tech. rep., Intergovernmental Panel on Climate Change (IPCC), https://doi.org/10.59327/IPCC/AR6-9789291691647, edition: First, 2023.

Forster, P., Storelvmo, T., Armour, K., Collins, W., Dufresne, J.-L., Frame, D., Lunt, D., Mauritsen, T., Palmer, M., Watanabe, M., Wild, M., and Zhang, H.: The Earth's Energy Budget, Climate Feedbacks and Climate Sensitivity, in: Climate Change 2021 – The Physical Science Basis: Working Group I Contribution to the Sixth Assessment Report of the Intergovernmental Panel on Climate Change [Masson-Delmotte, V., P. Zhai, A. Pirani, S.L. Connors, C. Péan, S. Berger, N. Caud, Y. Chen, L. Goldfarb, M.I. Gomis, M. Huang, K. Leitzell, E. Lonnoy, J.B.R. Matthews, T.K. Maycock, T. Waterfield, O. Yelekçi, R. Yu, and B. Zhou (eds.)], pp. 923–1054, Cambridge University Press, Cambridge, United Kingdom and New York, NY, USA, ISBN 978-1-009-15788-9, https://doi.org/10.1017/9781009157896.009, 2023.

Gierens, K.: Theory of Contrail Formation for Fuel Cells, Aerospace, 8, 164, https://doi.org/10.3390/aerospace8060164, 2021.

Graham, T.: On the law of the diffusion of gases, Journal of Membrane Science, pp. 17–21, https://doi.org/10.1016/0376-7388(94)00228-Q, 1995.

Gvakharia, A., Kort, E., Smith, M., and Conley, S.: Testing and evaluation of a new airborne system for continuous N2O, CO2, CO, and H2O measurements: the Frequent Calibration High-performance Airborne Observation System (FCHAOS), Atmospheric Measurement Techniques, 11, 6059–6074, https://doi.org/10.5194/amt-11-6059-2018, 2018.

Heller, R., Voigt, C., Beaton, S., Dörnbrack, A., Giez, A., Kaufmann, S., Mallaun, C., Schlager, H., Wagner, J., Young, K., and Rapp, M.: Mountain waves modulate the water vapor distribution in the UTLS, Atmospheric Chemistry and Physics, 17, 14 853–14 869, https://doi.org/10.5194/acp-17-14853-2017, 2017.

Hillenbrand, D. and Unterstrasser, S.: A new ice crystal formation pathway in contrails generated by fuel cell propelled aircraft, https://doi.org/10.5194/jecats-2026-16, 2026.

ICAO: Annex 16 to the Convention of International Civil Aviation Organization: Environmental protectionVol-II Aircraft Engine Emissions Fifth Edition, in: Vol-II Aircraft Engine Emissions Fifth Edition, Montreal, QC, Canada, https://elibrary.icao.int/product/329839, 2023.

Jansen, J. and Heymsfield, A. J.: Microphysics of Aerodynamic Contrail Formation Processes, Journal of the Atmospheric Sciences, 72, 3293–3308, https://doi.org/10.1175/JAS-D-14-0362.1, 2015.

Jurkat-Witschas, T., Voigt, C., Unterstraßer, S., Burkhardt, U., and Rapp, M.: Impact of Hydrogen in Aviation, ICAO Environmental Report, https://elib.dlr.de/216770/, 2025.

Kaufmann, S., Dischl, R., and Voigt, C.: Regional and seasonal impact of hydrogen propulsion systems on potential contrail cirrus cover, Atmospheric Environment: X, 24, 100 298, https://doi.org/10.1016/j.aeaoa.2024.100298, 2024.

Kitzis, D.: Preparation and Stability of Standard Reference Air Mixtures, https://gml.noaa.gov/ccl/airstandard.html, 2017.

Krysztofiak, G., Catoire, V., Dudok de Wit, T., Kinnison, D. E., Ravishankara, A. R., Brocchi, V., Atlas, E., Bozem, H., Commane, R., D'Amato, F., Daube, B., Diskin, G. S., Engel, A., Friedl-Vallon, F., Hintsa, E., Hurst, D. F., Hoor, P., Jegou, F., Jucks, K. W., Kleinböhl, A., Küllmann, H., Kort, E. A., McKain, K., Moore, F. L., Obersteiner, F., Ramos, Y. G., Schuck, T., Toon, G. C., Viciani, S., Wetzel, G., Williams, J., and Wofsy, S. C.: N2O Temporal Variability from the Middle Troposphere to the Middle Stratosphere Based on Airborne and Balloon-Borne Observations during the Period 1987–2018, Atmosphere, 14, 585, https://doi.org/10.3390/atmos14030585, number: 3, 2023.

Kulmala, M.: Condensational Growth and Evaporation in the Transition Regime, Aerosol Science and Technology, 19, 381–388, https://doi.org/10.1080/02786829308959645, 1993.

Kärcher, B.: Aviation-Produced Aerosols and Contrails, https://doi.org/10.1023/A:1006600107117, 1999.

Kärcher, B.: Formation and radiative forcing of contrail cirrus, Nature Communications, 9, 1824, https://doi.org/10.1038/s41467-018-04068-0, 2018.

Kärcher, B., Burkhardt, U., Bier, A., Bock, L., and Ford, I. J.: The microphysical pathway to contrail formation, Journal of Geophysical Research: Atmospheres, 120, 7893–7927, https://doi.org/10.1002/2015JD023491, 2015.

Lan, X., Thoning, K. W., and Dlugokencky, E. J.: Trends in globally-averaged CH4, N2O, and SF6 determined from NOAA Global Monitoring Laboratory measurements., version 2026-01, https://doi.org/10.15138/P8XG-AA10, 2026.

Lee, D., Fahey, D., Skowron, A., Allen, M., Burkhardt, U., Chen, Q., Doherty, S., Freeman, S., Forster, P., Fuglestvedt, J., Gettelman, A., De León, R., Lim, L., Lund, M., Millar, R., Owen, B., Penner, J., Pitari, G., Prather, M., Sausen, R., and Wilcox, L.: The contribution of global aviation to anthropogenic climate forcing for 2000 to 2018, Atmospheric Environment, 244, 117 834, https://doi.org/10.1016/j.atmosenv.2020.117834, 2021.

Lewellen, D. C.: A Large-Eddy Simulation Study of Contrail Ice Number Formation, Journal of the Atmospheric Sciences, 77, 2585–2604, https://doi.org/10.1175/JAS-D-19-0322.1, 2020.

Lottermoser, A. and Unterstrasser, S.: High-resolution modeling of early contrail evolution from hydrogen-powered aircraft, Atmospheric Chemistry and Physics, 25, 7903–7924, https://doi.org/10.5194/acp-25-7903-2025, publisher: Copernicus GmbH, 2025a.

Lottermoser, A. and Unterstrasser, S.: Towards intermediate complexity modelling of contrail formation: the new dynamical framework RadMod, The Aeronautical Journal, 129, 351–379, https://doi.org/10.1017/aer.2024.130, 2025b.

Lottermoser, A. and Unterstrasser, S.: Modeling the Impact of Alternative Fuels and Hydrogen Propulsion on Contrail-Cirrus: A Parameter Study, J. Geophys. Res., 131, e2025JD044 604, https://doi.org/10.1029/2025JD044604, 2026.

Mackay, C., Marizy, C., and Raguet, I.: The prediction of Ice SuperSaturated Regions and persistent contrail formation using weather data and in-flight observations, Proceedings of the 2024 Aeronautical Meteorology Scientific Conference (AeroMetSci-2024) p208, Publication AeM SERIES No. 10 WMO e-Library, https://library.wmo.int/idurl/4/69607, 2025.

Marsing, A., Meerkötter, R., Heller, R., Kaufmann, S., Jurkat-Witschas, T., Krämer, M., Rolf, C., and Voigt, C.: Investigating the radiative effect of Arctic cirrus measured in situ during the winter 2015–2016, Atmospheric Chemistry and Physics, 23, 587–609, https://doi.org/10.5194/acp-23-587-2023, 2023.

Mason, B. J.: The physics of clouds, Oxford : Clarendon Press, https://archive.org/details/physicsofclouds0000maso/page/n7/mode/2up, 1971.

Megill, L. and Grewe, V.: Investigating the limiting aircraft-design-dependent and environmental factors of persistent contrail formation, Atmospheric Chemistry and Physics, 25, 4131–4149, https://doi.org/10.5194/acp-25-4131-2025, 2025.

Moore, R. H., Thornhill, K. L., Weinzierl, B., Sauer, D., D'Ascoli, E., Kim, J., Lichtenstern, M., Scheibe, M., Beaton, B., Beyersdorf, A. J., Barrick, J., Bulzan, D., Corr, C. A., Crosbie, E., Jurkat, T., Martin, R., Riddick, D., Shook, M., Slover, G., Voigt, C., White, R., Winstead, E., Yasky, R., Ziemba, L. D., Brown, A., Schlager, H., and Anderson, B. E.: Biofuel blending reduces particle emissions from aircraft engines at cruise conditions, Nature, 543, 411–415, https://doi.org/10.1038/nature21420, 2017.

Märkl, R. S., Voigt, C., Sauer, D., Dischl, R. K., Kaufmann, S., Harlaß, T., Hahn, V., Roiger, A., Weiß-Rehm, C., Burkhardt, U., Schumann, U., Marsing, A., Scheibe, M., Dörnbrack, A., Renard, C., Gauthier, M., Swann, P., Madden, P., Luff, D., Sallinen, R., Schripp, T., and Le Clercq, P.: Powering aircraft with 100 % sustainable aviation fuel reduces ice crystals in contrails, Atmospheric Chemistry and Physics, 24, 3813–3837, https://doi.org/10.5194/acp-24-3813-2024, 2024.

Neumann, G., Marsing, A., Harlass, T., Sauer, D., Braun, S., Pühl, M., Heckl, C., Stock, P., De La Torre Castro, E., Hahn, V., Roiger, A., Voigt, C., Unterstraßer, S., Cammas, J., Renard, C., Vasenden, R., Vasenden, A., and Jurkat-Witschas, T.: In-flight emission measurements with an autonomous payload behind a turboprop aircraft, Atmospheric Measurement Techniques, 18, 6795–6816, https://doi.org/10.5194/amt-18-6795-2025, 2025.

O, K.-T. and Wood, R.: Exploring an approximation for the homogeneous freezing temperature of water droplets, Atmospheric Chemistry and Physics, 16, 7239–7249, https://doi.org/10.5194/acp-16-7239-2016, 2016.

Petters, M. D. and Kreidenweis, S. M.: A single parameter representation of hygroscopic growth and cloud condensation nucleus activity, Atmos. Chem. Phys., https://doi.org/https://doi.org/10.5194/acp-7-1961-2007, 2007.

Pitt, J. R., Le Breton, M., Allen, G., Percival, C. J., Gallagher, M. W., Bauguitte, S. J.-B., O'Shea, S. J., Muller, J. B. A., Zahniser, M. S., Pyle, J., and Palmer, P. I.: The development and evaluation of airborne in situ N_2O and CH_4 sampling using a quantum cascade laser absorption spectrometer (QCLAS), Atmospheric Measurement Techniques, 9, 63–77, https://doi.org/10.5194/amt-9-63-2016, 2016.

Ponater, M., Pechtl, S., Sausen, R., Schumann, U., and Hüttig, G.: Potential of the cryoplane technology to reduce aircraft climate impact: A state-of-the-art assessment, Atmospheric Environment, 40, 6928–6944, https://doi.org/10.1016/j.atmosenv.2006.06.036, 2006.

Ponsonby, J., King, L., Murray, B. J., and Stettler, M. E. J.: Jet aircraft lubrication oil droplets as contrail ice-forming particles, Atmospheric Chemistry and Physics, 24, 2045–2058, https://doi.org/10.5194/acp-24-2045-2024, 2024.

Ponsonby, J., Teoh, R., Kärcher, B., and Stettler, M. E. J.: An updated microphysical model for particle activation in contrails: the role of volatile plume particles, Atmospheric Chemistry and Physics, 25, 18 617–18 637, https://doi.org/10.5194/acp-25-18617-2025, 2025.

Prather, M. J., Hsu, J., DeLuca, N. M., Jackman, C. H., Oman, L. D., Douglass, A. R., Fleming, E. L., Strahan, S. E., Steenrod, S. D., Søvde, O. A., Isaksen, I. S. A., Froidevaux, L., and Funke, B.: Measuring and modeling the lifetime of nitrous oxide including its variability, Journal of Geophysical Research: Atmospheres, 120, 5693–5705, https://doi.org/10.1002/2015JD023267, 2015.

Riechers, B., Wittbracht, F., Hütten, A., and Koop, T.: The homogeneous ice nucleation rate of water droplets produced in a microfluidic device and the role of temperature uncertainty, Physical Chemistry Chemical Physics, 15, 5873, https://doi.org/10.1039/c3cp42437e, 2013.

Santoni, G. W., Lee, B. H., Wood, E. C., Herndon, S. C., Miake-Lye, R. C., Wofsy, S. C., McManus, J. B., Nelson, D. D., and Zahniser, M. S.: Aircraft Emissions of Methane and Nitrous Oxide during the Alternative Aviation Fuel Experiment, Environmental Science & Technology, 45, 7075–7082, https://doi.org/10.1021/es200897h, 2011.

Schulte, P. and Schlager, H.: In-flight measurements of cruise altitude nitric oxide emission indices of commercial jet aircraft, Geophysical Research Letters, 23, 165–168, https://doi.org/10.1029/95GL03691, _eprint: https://onlinelibrary.wiley.com/doi/pdf/10.1029/95GL03691, 1996.

Schumann, U.: On conditions for contrail formation from aircraft exhausts, Meteorologische Zeitschrift, pp. 4–23, https://doi.org/10.1127/metz/5/1996/4, 1996.

Schumann, U., Schlager, H., Arnold, F., Baumann, R., Haschberger, P., and Klemm, O.: Dilution of aircraft exhaust plumes at cruise altitudes, Atmospheric Environment, 32, 3097–3103, https://doi.org/10.1016/S1352-2310(97)00455-X, 1998.

Tian, H., Pan, N., Thompson, R. L., Canadell, J. G., Suntharalingam, P., Regnier, P., Davidson, E. A., Prather, M., Ciais, P., Muntean, M., Pan, S., Winiwarter, W., Zaehle, S., Zhou, F., Jackson, R. B., Bange, H. W., Berthet, S., Bian, Z., Bianchi, D., Bouwman, A. F., Buitenhuis, E. T., Dutton, G., Hu, M., Ito, A., Jain, A. K., Jeltsch-Thömmes, A., Joos, F., Kou-Giesbrecht, S., Krummel, P. B., Lan, X., Landolfi, A., Lauerwald, R., Li, Y., Lu, C., Maavara, T., Manizza, M., Millet, D. B., Mühle, J., Patra, P. K., Peters, G. P., Qin, X., Raymond, P., Resplandy, L., Rosentreter, J. A., Shi, H., Sun, Q., Tonina, D., Tubiello, F. N., van der Werf, G. R., Vuichard, N., Wang, J., Wells, K. C., Western, L. M., Wilson, C., Yang, J., Yao, Y., You, Y., and Zhu, Q.: Global nitrous oxide budget (1980–2020), Earth System Science Data, 16, 2543–2604, https://doi.org/10.5194/essd-16-2543-2024, 2024.

Voigt, C., Kleine, J., Sauer, D., Moore, R. H., Bräuer, T., Le Clercq, P., Kaufmann, S., Scheibe, M., Jurkat-Witschas, T., Aigner, M., Bauder, U., Boose, Y., Borrmann, S., Crosbie, E., Diskin, G. S., DiGangi, J., Hahn, V., Heckl, C., Huber, F., Nowak, J. B., Rapp, M., Rauch, B.,

Robinson, C., Schripp, T., Shook, M., Winstead, E., Ziemba, L., Schlager, H., and Anderson, B. E.: Cleaner burning aviation fuels can reduce contrail cloudiness, Communications Earth & Environment, 2, 114, https://doi.org/10.1038/s43247-021-00174-y, 2021.

Voigt, C., Märkl, R., Sauer, D., Dischl, R., Renard, C., Seeliger, K., Yu, F., Kaufmann, S., Bräuer, T., Jurkat-Witschas, T., Le Chenadec, G., Moreau, J., Requena-Esteban, E., Bonne, N., Vals, M., Roche, A., Zelina, J., Dörnbrack, A., Eirenschmalz, L., Heckl, C., Horst, E., Lichtenstern, M., Marsing, A., Neumann, G., Roiger, A., Scheibe, M., Stock, P., Giez, A., Eckel, G., and Le Clercq, P.: Substantial aircraft contrail formation at low soot emission levels, Nature, 652, 112–118, https://doi.org/10.1038/s41586-026-10286-0, 2026.

Waldmann, P., Eckl, M., Knez, L., Gottschaldt, K.-D., Fiehn, A., Mallaun, C., Gałkowski, M., Kiemle, C., Hutjes, R., Röckmann, T., Chen, H., and Roiger, A.: Quantifying agricultural N_2O and CH_4 emissions in the Netherlands using an airborne eddy covariance system, Atmospheric Measurement Techniques, 19, 185–210, https://doi.org/10.5194/amt-19-185-2026, 2026.

Zink, J. and Unterstrasser, S.: Contrail formation for aircraft with hydrogen combustion – Part 2: Engine-related aspects, Atmospheric Chemistry and Physics, 26, 3145–3165, https://doi.org/10.5194/acp-26-3145-2026, 2026.

Zink, J., Unterstrasser, S., and Jurkat-Witschas, T.: On the Potential Role of Lubrication Oil Particles in Contrail Formation for Kerosene and Hydrogen Combustion, Journal of Geophysical Research: Atmospheres, 130, e2025JD043 487, https://doi.org/10.1029/2025JD043487, _eprint: https://agupubs.onlinelibrary.wiley.com/doi/pdf/10.1029/2025JD043487, 2025.

Zink, J., Unterstrasser, S., and Burkhardt, U.: Contrail formation for aircraft with hydrogen combustion – Part 1: A systematic microphysical investigation, Atmospheric Chemistry and Physics, 26, 3125–3143, https://doi.org/10.5194/acp-26-3125-2026, 2026.